

國立臺灣大學理學院物理學研究所

碩士論文

Graduate Institute of Physics

College of Science

National Taiwan University

Master Thesis



研究 2018 Test Beam 中 HGICAL (高粒度量能器) 能量重建  
之能力表現

CMS HGICAL prototype EM Energy Reconstruction  
Performance in a 2018 Test Beam

蘇俊瑋

Jyun-Wei Su


指導教授：裴斯達 博士

Advisor: Stathes Paganis, Ph.D.

中華民國 109 年 8 月

August, 2020

## 摘要



世界上最大且能量最高的粒子加速器-大強子對撞機(LHC)，正準備進入「高亮度」(High Luminosity)的時代。在下一個階段的運行過程中，LHC會產生10倍於前階段的累積亮度(integrated luminosity)，其中的偵測器將會面臨兩個重大挑戰:輻射損傷以及碰撞點產生的事件數上升導致對單一事件的分析產生困難。高粒度量能器(HGCAL)作為緊湊渺子線圈實驗(CMS)的其中一項升級，高粒度量能器將會取代現有量能器兩端電磁量能器及強子量能器的部分。電磁量能器與大部分的強子量能器會採用0.5~1平方公分大小的矽感應器，矽感應器精確的時間測量能力可以幫助分辨出短時間內產生的大量事件。本論文將以2018的粒子測試資料為主，研究2018模組的非均一性(non-uniformity)以及資料與蒙地卡羅模擬(Monte Carlo)之間是否存在差異性(非均一性)。本論文中我們測得在真實數據中的固定項(constant term)為 $0.82 \pm 0.14\%$ 而隨機項(stochastic term)為 $22.59 \pm 0.72\%$ ；而Monte Carlo中則分別為 $0.86 \pm 0.01\%$ 及 $22.91 \pm 0.07\%$ 。由此我們可以推論出真實數據和Monte Carlo有高度的一致性。我們也在真實數據和Monte Carlo中分別看到 $0.89 \pm 0.08\%$ 和 $0.61 \pm 0.05\%$ 的非均一性，兩者存在約 $0.65 \pm 0.06\%$ 的差異性。

關鍵字: 粒子物理、高能物理、量能器、偵測器、能量重建。

## Abstract

The LHC, which is the largest and highest energy particle accelerator in the world, is preparing to step into the new era of high luminosity. The LHC will generate 10 times more integrated luminosity than now. Thus, the detectors in the LHC are going to face two big challenges: the radiation damage and the difficulty in analysis caused by event pileup. The High-Granularity Calorimeter technology is one of many upgrades of the CMS in phase-2 upgrading program, it will replace the existing endcap calorimeters, including the electromagnetic and hadronic sections. The EM calorimeters and a large proportion of hadronic calorimeter will use silicon sensors of  $0.5\sim 1\text{cm}^2$  which have high accuracy of timing capacity that is helpful to pileup rejection.

This thesis is based on the test beam data in 2018. The main interest for the future HGCal operation at LHC is in maintaining a low C-term below 1%. Energy non-uniformity effects impact directly the C-term and the information provided in this Thesis gives a first glimpse on the magnitude of these effects. In this thesis we found a constant term and stochastic term of  $0.82 \pm 0.14\%$ ,  $22.59 \pm 0.72\%$  for data and  $0.86 \pm 0.01\%$ ,  $22.91 \pm 0.07\%$  for Monte-Carlo (MC) respectively. The MC is in a good agreement with data. We also found a non-uniformity  $0.89 \pm 0.08\%$  for data and  $0.61 \pm 0.05\%$  for MC, which corresponds to a  $0.65 \pm 0.06\%$  mismatch between data and MC.

**Keywords:** *Particle physics, High energy physics, Calorimeter, Detector, Energy reconstruction*

# Contents



|          |  |           |
|----------|--|-----------|
| <b>1</b> | <b>Introduction</b>  | <b>1</b>  |
| 1.1      | Energy loss of particle in matter . . . . .                    | 1         |
| 1.1.1    | Minimum ionizing particle (MIP) . . . . .                      | 3         |
| 1.2      | Particle showers . . . . .                                     | 3         |
| 1.2.1    | Electromagnetic shower . . . . .                               | 4         |
| 1.2.2    | Hadronic showers . . . . .                                     | 5         |
| 1.3      | Calorimeters in particle physics . . . . .                     | 6         |
| 1.3.1    | Performance of electromagnetic calorimeters . . . . .          | 6         |
| <b>2</b> | <b>The CMS experiment at Large Hadron Collider</b>             | <b>8</b>  |
| 2.1      | The colliding proton beams and bunches . . . . .               | 8         |
| 2.2      | Accelerating the beam . . . . .                                | 8         |
| 2.3      | LHC Magnets . . . . .  | 9         |
| 2.4      | The CMS experiment . . . . .                                   | 10        |
| 2.4.1    | Coordinate system of the CMS detector . . . . .                | 12        |
| 2.4.2    | Magnet configuration . . . . .                                 | 12        |
| 2.4.3    | Tracking system . . . . .                                      | 13        |
| 2.4.4    | Electromagnetic calorimeter (ECAL) . . . . .                   | 14        |
| 2.4.5    | Hadronic calorimeter (HCAL) . . . . .                          | 15        |
| 2.4.6    | Muon detector . . . . .  | 16        |
| 2.4.7    | Trigger system . . . . .                                       | 17        |
| <b>3</b> | <b>The HGAL upgrade for the CMS phase 2</b>                    | <b>18</b> |
| 3.1      | Silicon as active material in a sampling calorimeter . . . . . | 19        |
| 3.2      | Overview of HGAL . . . . .                                     | 21        |
| <b>4</b> | <b>HGAL beam-test prototypes</b>                               | <b>24</b> |
| 4.1      | HGAL modules . . . . .   | 24        |
| 4.2      | 2018 beam-test setup . . . . .                                 | 26        |
| 4.2.1    | HGAL Prototype . . . . .                                       | 30        |
| 4.2.2    | Trigger and DAQ systems . . . . .                              | 32        |
| <b>5</b> | <b>Electron energy reconstruction</b>                          | <b>33</b> |
| 5.1      | The dEdx method . . . . .                                      | 33        |
| 5.2      | The sampling fraction method . . . . .                         | 35        |
| 5.3      | EM calorimeter energy resolution . . . . .                     | 36        |
| 5.4      | Stochastic term . . . . .                                      | 36        |



|          |  |           |
|----------|--|-----------|
| 5.5      | Electron energy reconstruction . . . . . | 37        |
| <b>6</b> | <b>Uniformity Study</b>                  | <b>41</b> |
| <b>7</b> | <b>Conclusion</b>                        | <b>62</b> |



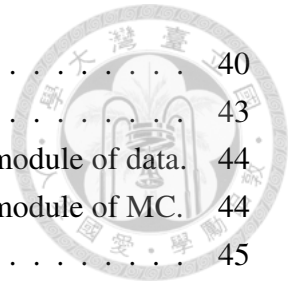
## List of Tables

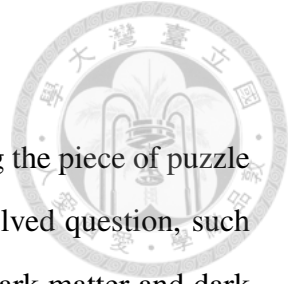
|   |  |    |
|---|--|----|
| 1 | Relation between pseudorapidity and angle. . . . .                                   | 12 |
| 2 | H2 beamline positron beam momentum and momentum spreads. . . . .                     | 28 |
| 3 | The beam energy and corresponding run number. . . . .                                | 38 |
| 4 | The MPV of data $E_{visible}(E^{Si})$ in different pads with different energies. . . | 54 |
| 5 | The MPV of MC $E_{visible}(E^{Si})$ in different pads with different energies. . .   | 54 |
| 6 | The stochastic terms and constant terms of different pads in data and MC. .          | 56 |

## List of Figures

|     |   |    |
|-----|---|----|
| 1.1 | $-\langle \frac{dE}{dx} \rangle$ of Moun, Pion and Proton [1] . . . . . | 2  |
| 2.1 | Structure of LHC . . . . .  | 10 |
| 2.2 | Schematic of the CMS experiment [2] . . . . .                           | 11 |
| 2.3 | Structure of the tracking system [2] . . . . .                          | 13 |
| 2.4 | Structure of the ECAL [2] . . . . .                                     | 14 |
| 2.5 | Structure of the HCAL [2] . . . . .                                     | 15 |
| 2.6 | Structure of the Muon Detector [3] . . . . .                            | 16 |
| 2.7 | Architecture of CMS level 1 (L1) trigger system. [2] . . . . .          | 17 |
| 3.1 | LHC upgrading schedule. [4] . . . . .                                   | 18 |
| 3.2 | Material design for HGCAL. [5] . . . . .                                | 21 |
| 3.3 | Longitudinal structure of the HGCAL. . . . .                            | 23 |
| 4.1 | CE-E silicon module, showing stacked layers. [6] . . . . .              | 24 |
| 4.2 | Sensor design. [5] . . . . .  | 25 |
| 4.3 | The complete module of the 2017/2018 . . . . .                          | 26 |
| 4.4 | H2 beamline flexible magnetic spectrometer. . . . .                     | 27 |
| 4.5 | H2 beamline and HGCAL-prototype experimental setup. . . . .             | 28 |
| 4.6 | Delay wire chamber and supporting frame. . . . .                        | 29 |
| 4.7 | Layout for the CE-E prototype. . . . .                                  | 31 |
| 4.8 | Test beam CE-E and CE-H setup. . . . .                                  | 32 |
| 5.1 | Reconstruction energy $E_{rec}$ distribution. . . . .                   | 38 |
| 5.2 | Energy linearity and resolution of MC. . . . .                          | 39 |

|     |   |    |
|-----|---|----|
| 5.3 | Linearity plot of Data and MC. . . . .  | 40 |
| 6.1 | Distribution of event position. . . . .   | 43 |
| 6.2 | The schematic diagram of pad location and number on the module of data. . . . . | 44 |
| 6.3 | The schematic diagram of pad location and number on the module of MC. . . . .   | 44 |
| 6.4 | The distribution of $E_{visible}$ in different pads. . . . .                    | 45 |
| 6.5 | The resolution plot of all pads and single pad for data and MC. . . . .         | 55 |
| 6.6 | Constant term vs stochastic term for different pads. . . . .                    | 56 |
| 6.7 | $E_{rec}$ deviation for different pads. . . . .                                 | 60 |
| 6.8 | The distribution of the deviations from different pads in all energy. . . . .   | 61 |





# 1 Introduction

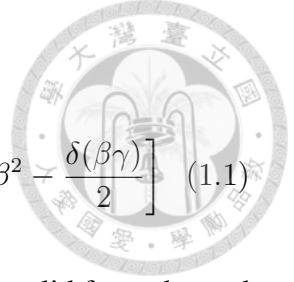
While the Large Hadron Collider (LHC) completed the task of finding the piece of puzzle of the Standard Model, the Higgs boson, there are still many unresolved questions, such as the origin of the Higgs boson, the CP violation, the existence of dark matter and dark energy, failure of uniting the gravitation with the rest known interaction, etc.

Detector technology plays a vital role in collecting and selecting data of interesting physics events. We study physical phenomena by reconstructing and analyzing the physics events. In this process, measured quantities are, the position, momentum and the energy of produced particles. These observables are reconstructed by several detectors operating in the same experiments. The calorimeter is responsible for measuring energy, it plays an imperative role in particle physics experiments. In this chapter the interaction of radiation with matters is briefly discussed. The principal of Calorimetry are also introduced.

## 1.1 Energy loss of particle in matter

In high energy physics experiments, measuring energy loss of particle in certain material is an important task. After a particle gets in the detector, it undergoes some interactions and deposits some energy in the material. By observing the loss of energy of particles during interaction, we can retrieve information about the original particle, such as Particle ID, energy, direction, etc.

When a charged particle goes through matter, it interacts with atomic electron and excites or ionizes the atoms of the matter, leading to energy loss of the traveling particle. By taking account of quantum mechanics and relativistic effects, Hans Bethe and Felix Bloch deduced the Bethe-Bloch formula that gives a good description of the mean rate of energy loss of a heavy charged particle ( $M_{incident} \gg M_{electron}$ ) passing through matter. The Bethe-Bloch formula is shown below:



$$\left\langle -\frac{dE}{dx} \right\rangle \approx \frac{4\pi}{m_e c^2} \cdot \frac{n_e Z_i^2}{\beta^2} \cdot \left( \frac{e^2}{4\pi\epsilon_0} \right)^2 \cdot \left[ \frac{1}{2} \ln \left( \frac{2m_e c^2 \beta^2 \gamma^2 T_{max}}{I^2} \right) - \beta^2 - \frac{\delta(\beta\gamma)}{2} \right] \quad (1.1)$$

This formula can be applied in the region  $0.1 \lesssim \beta\gamma \lesssim 1000$  and is valid for a charged particle with velocity  $v(= \beta c)$ , spin 0 and charge  $Z_i$  electron charge traveling through material with atomic number  $Z$ , electron density  $n_e$  and mean ionization potential  $I$ .  $T_{max}$  is the maximum kinetic energy can be imparted to an electron in a single collision by traveling particle. The  $\delta(\beta\gamma)$  term stands for the density-effect correction causes by the polarization of matter. The effect of the formula is shown in Fig 1.1.

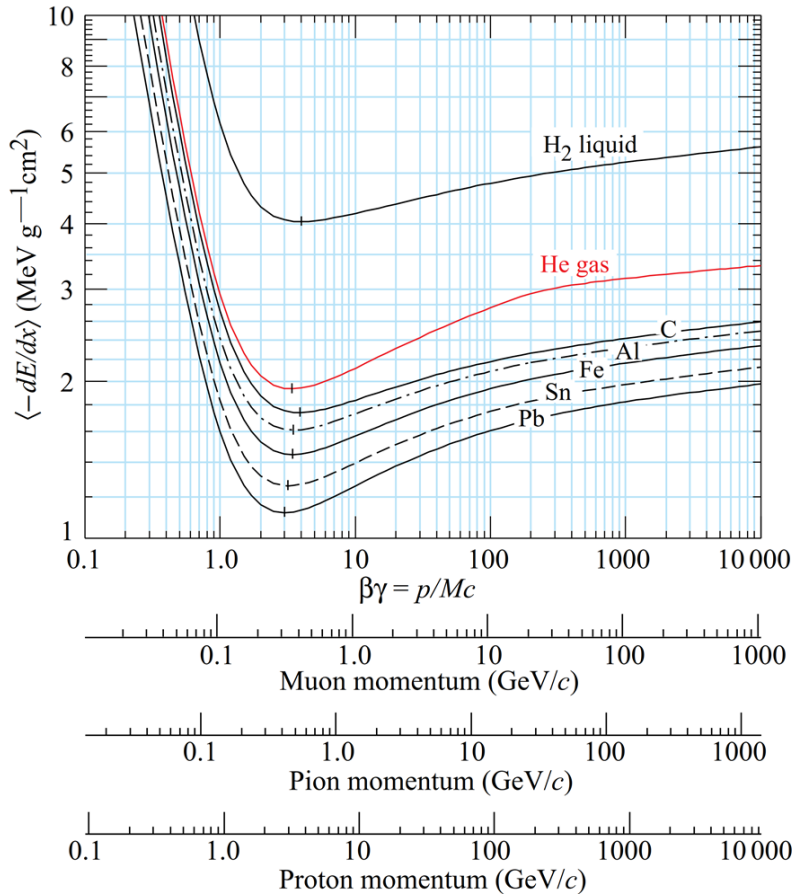
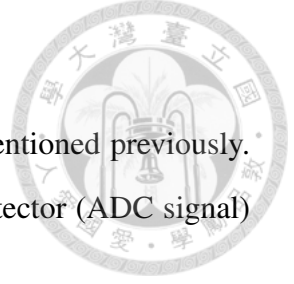


Figure 1.1:  $-\langle \frac{dE}{dx} \rangle$  of Moun, Pion and Proton [1]

As shown in the plot, there is a minimum point of the formula independent of particle type. A Particle in this region is called minimum ionizing particle (MIP).



### 1.1.1 Minimum ionizing particle (MIP)

The concept of MIP is based on the Bethe-Bloch equation as we mentioned previously. Due to its special property, we use MIP to calibrate the signal of detector (ADC signal) with real physics data.

In practice, muons are usually treated as MIP particles, because muons do not produce showers in material but mainly participate through the interaction of ionization.

We know that the average energy loss of a charged particle passing through matter is well described by Bethe-Bloch formula, while the Landau distribution describes the fluctuations of energy loss by ionization of charged particle in a thin layer of matter. During the penetration, a small part of particles transfers more energy. These events mainly came from head-on collision of atomic electron or nuclear interaction. So, instead of Gaussian distribution, the energy loss distribution has a tail toward high energy.

The most probable value of the energy loss in a material with thickness  $x$  is

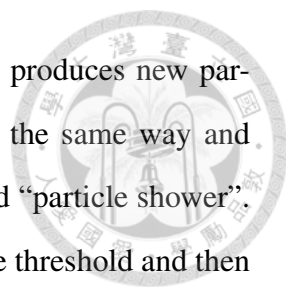
$$W_{mp} = \xi \left( \ln \frac{\xi}{\epsilon'} + 0.198 - \delta \right), \text{ with } \xi = \frac{2\pi n_e Z_i^2 e^4}{mv^2} x \quad (1.2)$$

Where  $\sigma$  is the density effect of the material and the  $\epsilon'$  is the cutoff on low energy transfer for a single interaction. The  $\epsilon'$  was chosen by Landau so that mean energy loss will agree with Bethe-Bloch formula.[7]

## 1.2 Particle showers

At low energy, the energy loss of charged particles is dominated by ionization as mentioned previously. However, for energy higher than “critical energy”  $E_c$ , the main energy loss is dominated by braking radiation or bremsstrahlung in German. The critical energy with charge  $Z$  of the nucleus is approximately

$$E_c \sim \frac{800}{Z} \text{ MeV.} \quad (1.3)$$



In this energy scale, incoming particle interacts with matter and produces new particles with lower energy. The newly produced particles interact in the same way and produce a cascade of secondary particles. The whole process is called “particle shower”. The shower process will last until energy of all particles are below the threshold and then the shower slowly dies out as particles absorbed by matter.

Because of the difference of incident particles, particle showers can be separated into two parts: electromagnetic showers and hadronic shower. The former is produced by particles interacting primarily via the electromagnetic interaction, such as electrons and photons. The latter is produced by hadrons, which mostly interact via the strong interaction. Hence calorimeters are usually designed into two parts: electromagnetic part and hadronic part.

### 1.2.1 Electromagnetic shower

When a high-energy electron interacts with in a medium it radiates bremsstrahlung-photon, and then the high-energy photon produce an electron and positron pair via pair production. This process continues to produce a cascade of photons, electrons and positrons, refers to as an electromagnetic shower.

Here we need to mention a parameter that can be used to estimate the EM shower, the radiation length  $X_0$ . The radiation length is the average distance that the energy of electron is reduced via bremsstrahlung by  $1/e$ , where  $e$  is base of natural logarithm. Due to this definition, the distance of a high-energy photon reduce its energy by  $1/e$  is approximately  $9/7 X_0$ . The  $X_0$  can be approximated by the expression

$$X_0 = \frac{716.4A}{Z(Z+1)\ln(287/Z^{1/2})} \cdot \frac{1}{\rho} \text{ (cm)} \quad (1.4)$$

In electromagnetic shower, the number of particles doubles after every radiation length of material passed. Therefore, in an electromagnetic showers produced by electron or photon with energy  $E$ , the average energy of particles after  $x$  radiation lengths is

$$\langle E \rangle \approx \frac{E}{2^x} \quad (1.5)$$

The shower continues to develop until the average energy of particles gets below the critical energy. At this point the electromagnetic shower has maximum particle number after  $x_{max}$  radiation lengths, with  $\langle E \rangle \approx E_c$ . From equation (1.5) we get

$$x_{max} = \frac{\ln(E/E_c)}{\ln 2} \quad (1.6)$$

The lateral information can be described by Molière radius  $R_M$ , it contains 90% of the shower. The Molière radius can be approximated by

$$R_M = \frac{21.2}{E_c} X_0 \quad (1.7)$$

Using these parameter, we can design the electromagnetic part of a calorimeter.

### 1.2.2 Hadronic showers

Hadronic showers are produced by strong interaction between the incident particles and nucleus, which can be described by quantum chromodynamics (QCD). The secondary particles produced by strong interaction can be separated into the electromagnetic part (productions of  $\pi^0$ ) and hadronic part ( $p, n, \pi^+$ ). About half of energy of incident hadron pass on to secondary particles, the remainder will dissipate in multiparticle production of slow pions and in other process.

Because the strong interaction has small cross-section, hadronic showers always begin in deeper parts in calorimeter, and have much broader spread than EM showers. Hence the design of the hadronic part of calorimeter has typically thicker absorber and is placed behind the EM part.

We use interaction length ( $\lambda_I$ ) to describe the behavior of hadronic shower, which related to the mean free path of a particle traveling in nuclear sea. The definition of  $\lambda_I$  is



$$\lambda_I = \frac{A}{N_A \sigma_{total}} \quad (1.8)$$

where  $A$  is atomic weight,  $N_A$  is Avogadro constant and  $\sigma_{total}$  is the total cross section for the strong interaction.

### 1.3 Calorimeters in particle physics

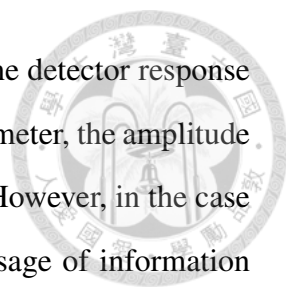
The calorimeter is designed to absorb the energy of an incident particle and transform it to a measurable quantity, such as charge and light, so that we can reconstruct the original energy. The calorimeter can measure the energy of electrons, photons,  $\tau$ s and jets along with identifying the muon tracks. With hermetic calorimeter, we can even reconstruct the missing transverse energy of an event.

Most of calorimeters are position sensitive, usually they are segmented and have independent signal readout. In the lateral geometry the calorimeters can be categorized as homogeneous calorimeters and sampling calorimeters. For homogeneous calorimeters, they are only segmented in the lateral direction, so one segment absorbs energy and provides measurable signal at the same time. For sampling calorimeters, it has both lateral and longitudinal segments. There are two types of layers in sampling calorimeter. The absorber layer is usually composed of passive, dense material with high atomic number. It absorbs most of the energy and induces showering. The active layer is responsible for measuring signal and energy. While almost all energy is converted into signal in a homogeneous calorimeter, only a fraction of energy contributes measured energy signal in a sampling calorimeter.

#### 1.3.1 Performance of electromagnetic calorimeters

We can evaluate the performance of EM calorimeters through many aspects, such as the precision of energy measurement, the degradation of active material after radiation damage, power consumption of detector, etc. Here we only focus on EM calorimeters.





The first criterion is the linearity of detector. Linearity refers to the detector response being linear for a range of energy of interest. For homogeneous calorimeter, the amplitude of collected signal is proportional to the energy of incident particle. However, in the case of sampling calorimeter, there are different methods based on the usage of information obtained from the slice of shower. For example, we can give each active layer a corresponding weight; estimating the MIP number of each active can be used as a tool to trace back the energy lost in an absorb layer. Identifying particles from the measured shower shape can also help in energy reconstruction.

Another important parameter in a calorimeter is the energy resolution, usually defined as  $\sigma_E/E$  for a given beam energy  $E$ , where  $\sigma_E$  is the Gaussian Std deviation of the reconstructive Energy distribution. The dominant term in energy resolution is usually related to sampling fluctuation, which is Poisson distribution in nature. We will explain this in detail in Chapter 5.

## 2 The CMS experiment at Large Hadron Collider

The Large Hadron Collider (LHC) is a high energy particle collider at European Laboratory for Particle Physics (CERN), straddles the border between France and Switzerland just outside Geneva. The LHC, largest experimental device in the world, is now lying 175 meters underground with a circumference 26.7 km, using the tunnel used to served Large Electron Positron (LEP).

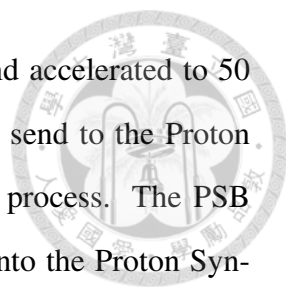
The LHC is designed to deliver proton-proton collisions at center of mass energy 13 to 14 TeV, it can also deliver lead-lead or proton-lead heavy-ion collisions. The Compact Muon Solenoid (CMS) is 1 of 4 main experiments in LHC, which are ATLAS, (CMS), ALICE and LHCb. Among these, ATLAS and CMS are general-purpose detectors (GPD) designed for high luminosity and searches in a wide variety of channels. In this chapter, we will have a brief introduction of LHC and CMS.

### 2.1 The colliding proton beams and bunches

The main task of the LHC is producing two proton beams in opposite direction circulate in beam pipe then collide at interaction point. The Beam is divided into maximum 2800 bunches. Each bunch is about 30 cm long and the having a horizontal spread about  $20\mu m \sim mm$ , and there are approximately  $1.15 \times 10^{11}$  protons inside. Bunches are separated at a bunch spacing of 25 ns ( $\sim 7.5 m$ ). Due to frequent collision-rate and high density of beam, the average luminosity is reach up to an order of  $10^{34} cm^{-2}s^{-1}$ . When bunches pass through each other, the number of collision is defined as “pileup”, and during 2015 to 2018, the pileup is estimated to be 25~60. [8]

### 2.2 Accelerating the beam

Before the energy of proton beams reach the energy we desire, these bunches need to undergo multiple stage of acceleration. The first stage takes place in Linear accelerator 2 (LINAC2). The protons are produced by sending Hydrogen gas into electric field to



remove their electron, then the protons are injected into LINAC2 and accelerated to 50 MeV energy scale. In second stage, the bunches from LINAC2 are sent to the Proton Synchrotron Booster (PSB), which is the first accelerator in whole process. The PSB raises the energy from 50 MeV to 1.4 GeV and inject the bunches into the Proton Synchrotron (PS). The PS further increases the up to 25 GeV and then inject the bunches into Super Proton Synchrotron (SPS). The SPS is the final stage before beam get into the LHC. The beam is accelerated to 450 GeV in here. The LHC raise the beam energy up to 6.5 TeV, which is approximately 99.999999% of light speed, and separate the beam into two opposite directions prepare for collision.

### **2.3 LHC Magnets**

Another important part in the LHC is magnets, more than 50 types of magnets are used. The magnets in LHC can be separated in two kinds: the lattice magnets and the insertion magnets. Thousands of magnets are used to bend and tighten the particles' trajectory. They are responsible for keeping the beams stable and precisely aligned.

Dipole magnets is one of the most complex parts in LHC, they are used to bend the path of particles. There are 1232 main dipoles, each. 15 meters long and 35 tons weight. Quadrupoles are used to keep the particles in tight beam. They have four magnetic poles arranged symmetrically around the beam pipe to squeeze the beam.

When beam enter the detectors, the insertion magnets take over. Before particles collide, they must be squeezed closer together for higher collide rate. The inner triplets, which are made up of three quadrupoles, located at each of four larger LHC detectors, ALICE, ATLAS, CMS and LHCb. The inner triplets tighten the beam, make it 12.5 times narrower. After beams collide in the detector, via the magnetic field created by enormous magnets, we can determine the identity of the particles. When it is time to dispose the particles, a dilution magnet lower the intensity by level of 100,000 before the beam collides the beam dump.



## CERN's Accelerator Complex

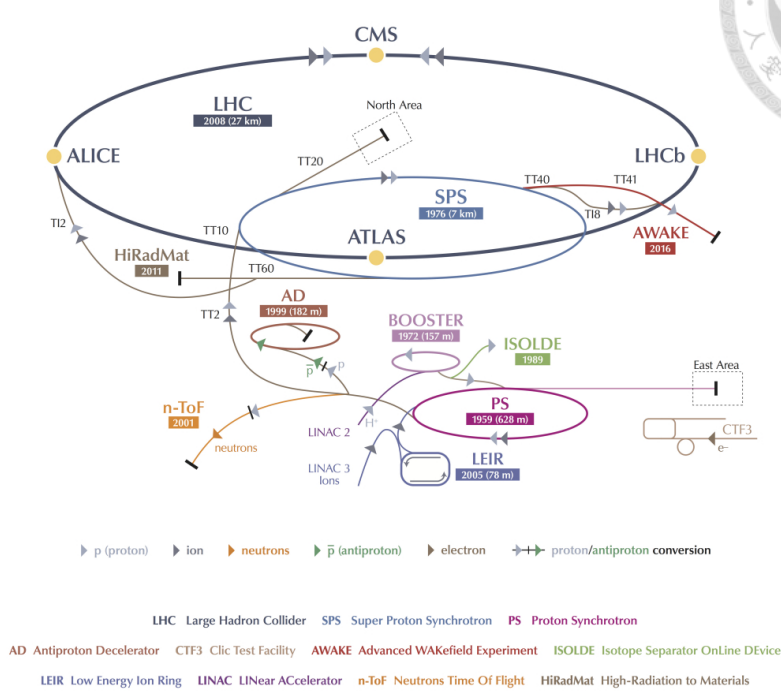


Figure 2.1: Structure of LHC

## 2.4 The CMS experiment

The compact muon solenoid is one of two general-purpose detectors in LHC, located at one of the collision points. It's used to measure the momentum and energy of long-lived particles created by the collision. The primary goal of CMS includes studying standard model (search of Higgs boson), probing the physics beyond standard model such as supersymmetry and extra dimensions, even revealing the truth of the dark matter and dark energy.

The CMS weighs double than ATLAS, but only occupies one eights of ATLAS volume, the fact is reflected by the word “compact”. The CMS is a hollowed cylinder, with 15 meters high, 21 meters long, and weighs 12,500 tons. CMS comprises over 100 million individual detector elements.

The center part of the CMS is an enormous superconducting solenoid, which is the biggest magnet of the kind ever built. It is a cylindrical superconducting coil capable

to create a magnetic field of 4T. The magnetic field bends the trajectories of charged particles to enable momentum measurement. The silicon trackers located outside the superconducting solenoid, very close to the collision point. The silicon tracker is used to tracking charged particles and helping to measure their momentum. The tracker can also indicate the points in space where long-lived particles decay. The calorimeters are placed outside the tracker system, which is used to measure the energy of particles. Finally, the outermost part is the muon detectors, which provide the information of muon.

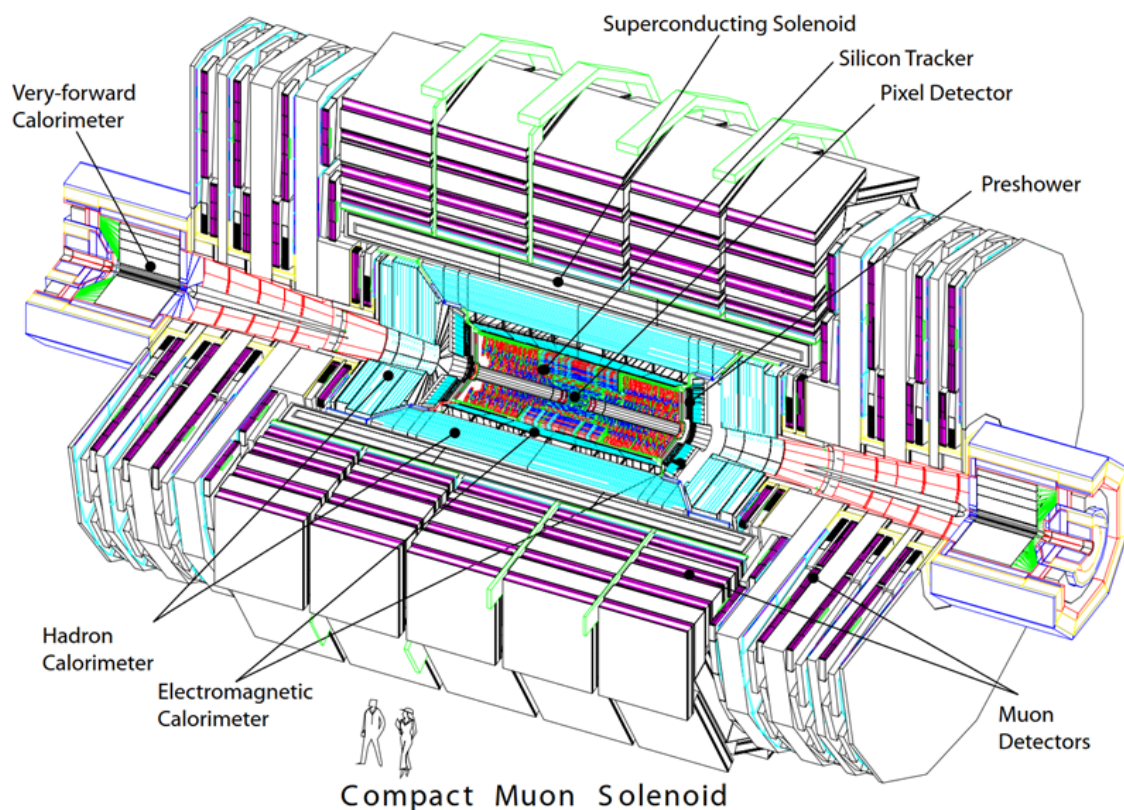
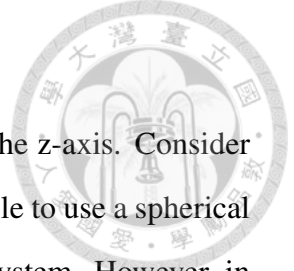


Figure 2.2: Schematic of the CMS experiment [2]



### 2.4.1 Coordinate system of the CMS detector

Due to the cylindrical structure of the CMS, which is symmetric in the z-axis. Consider the physics events are generated from the interaction point, it is suitable to use a spherical coordinate system to describe both physics events and the detector system. However, in the hard process occurring at the TeV scale, the center-of-mass of the event is possibly to be boosted along the z-axis, which is no longer Lorentz-invariant. Thus, a Lorentz-invariant measure, the rapidity( $y$ ), is introduced:

$$y \equiv \frac{1}{2} \ln\left(\frac{E + cp_z}{E - cp_z}\right) \tag{2.1}$$

The  $E$  is the energy of the final state,  $p_z$  is the momentum along z-axis.

Moreover, if the energy of the final state is high compare to rest mass of particle in a hard process of TeV scale, namely  $E^2 \gg mc^2$ , the approximation  $E \rightarrow c|p|$  can be applied, which gives a new measure called the pseudorapidity ( $\eta$ )

$$\eta \equiv -\ln\left(\tan\left(\frac{\theta}{2}\right)\right)$$

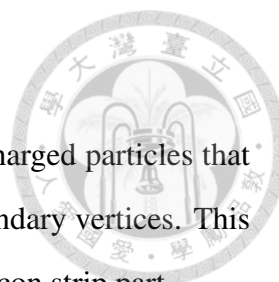
The  $\theta$  is the polar angle measured from the beam axis. In LHC we use pseudorapidity to replace polar angle. The following is some transforms between pseudorapidity and angle

|          |          |      |      |      |      |      |      |       |    |
|----------|----------|------|------|------|------|------|------|-------|----|
| $\theta$ | 0        | 5    | 10   | 20   | 30   | 45   | 60   | 80    | 90 |
| $\eta$   | $\infty$ | 3.13 | 2.44 | 1.74 | 1.31 | 0.88 | 0.55 | 0.175 | 0  |

Table 1: Relation between pseudorapidity and angle.

### 2.4.2 Magnet configuration

The superconducting coil is designed to generate  $4T$  magnetic fields, but during operation is  $3.8T$ . The magnetic field can help to bend the trajectory of the charged particles so that we can measure their momentum.



### 2.4.3 Tracking system

The tracking system of the CMS aims to measure the trajectory of charged particles that created by collision and provides information to reconstruct the secondary vertices. This sub-system is silicon-based and is composed of the pixel part and silicon strip part.

Silicon pixel detector locate at the inner-most region of tracking system, it's designed to be size of shoebox. In the original design, the 2D sensor components are  $100 \times 150\mu\text{m}$  cells. With such fine 2D cells and a coverage up to  $|\eta| \sim 2.5$ , the detector can provide very high spatial resolution about  $15 \sim 20\mu\text{m}$  around the interaction point.

The strip detectors are composed of three different sub-systems: the Tracker Inner Barrel and Disks (TIB/ TID), the Tracker Outer Barrel (TOB) and the Tracker End-Caps (TEC). The strip detectors are placed outside the pixel detectors (shown in Figure 2.3). In the inner region ( $20\text{cm} < r < 55\text{cm}$ ), strips with 10cm long and  $80\mu\text{m}$  wide are used. While in the outer region ( $55\text{cm} < r < 110\text{cm}$ ) the strip pitch is further loosen. Silicon with different thickness is also applied due to the radiation flux of different position, e.g.  $500\mu\text{m}$  in the outer tracker and  $320\mu\text{m}$  in the inner tracker.

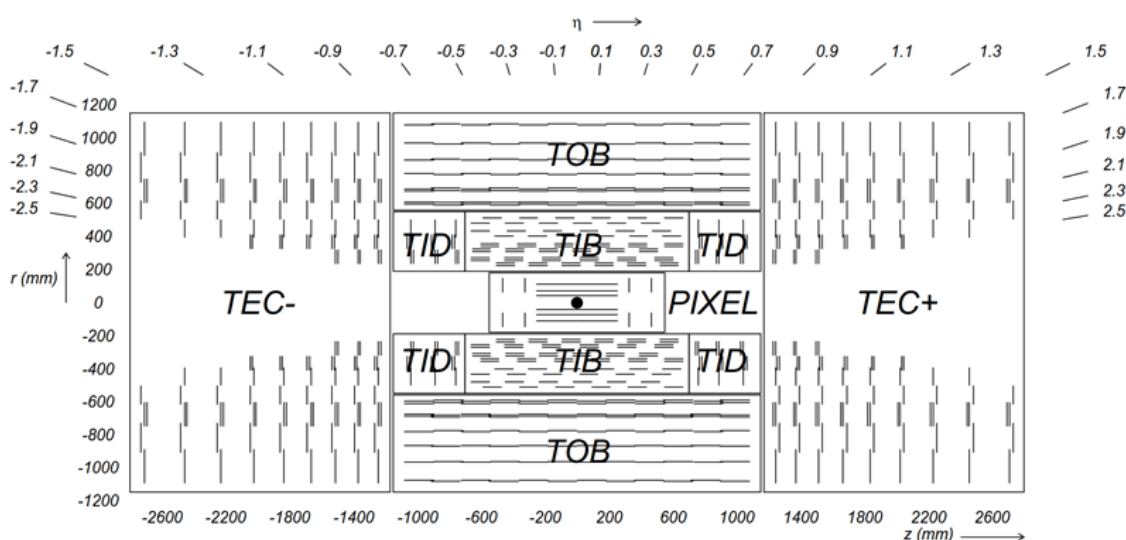
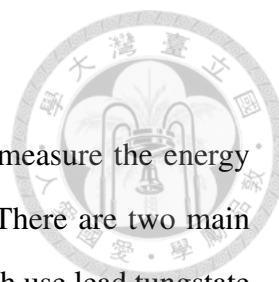


Figure 2.3: Structure of the tracking system [2]



## 2.4.4 Electromagnetic calorimeter (ECAL)

The electromagnetic calorimeter (ECAL), a sub-system, is used to measure the energy of particles that undergo through electromagnetic shower process. There are two main part of ECAL: the barrel part (EB) and the end-cap part (EE), they both use lead tungstate ( $PbWO_4$ ) crystals as material for detecting. There is a preshower detector placed in front of the EE part shown in Figure 2.4.

The reason we use lead tungstate as scintillating crystal is because of its high density ( $8.28g/cm^3$ ), short radiation length ( $X_0 = 0.89cm$ ), low Molière radius ( $R_m = 2.2cm$ ), fast scintillation response (25 ns), optical transparency and radiation hardness. But the disadvantage of lead tungstate is the scintillation rate is highly temperature related. Thus, the operation temperature must maintain at  $18 \pm 0.1^\circ C$ . The EB part covers the region  $|\eta| < 1.479$ , with the crystal cross-section  $\approx 0.0174 \times 0.0174$  in  $\eta - \phi$ . The EE part covers the region  $1.653 < |\eta| < 3.0$ . The crystals in EB part are 230 mm long, which corresponding to  $25.8X_0$ , for the EE part the length is 220 mm ( $24.7X_0$ ).

The Preshower detector (ES) covers the region  $1.653 < |\eta| < 2.6$ . It is made of two planes of lead and followed by silicon sensors, and the width of the preshower strips are 2mm. The aim of the Preshower detector is to identify neutral pions in the end-cap, and it can also help the identification of electrons against MIPs while improving the position determination at the same time.

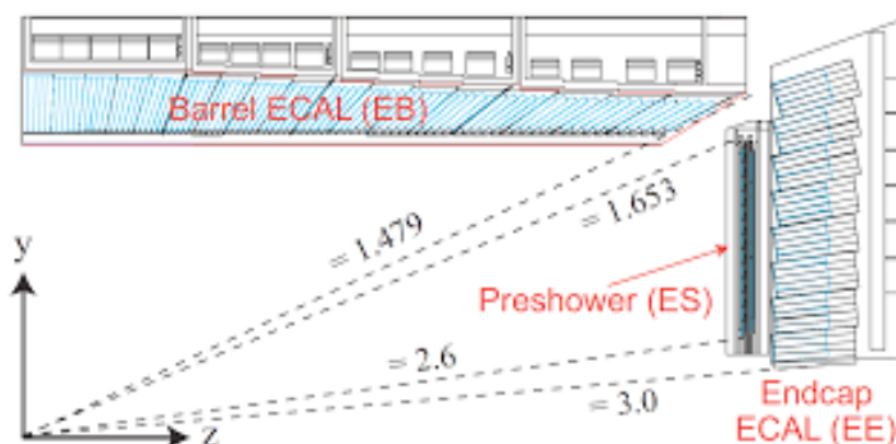
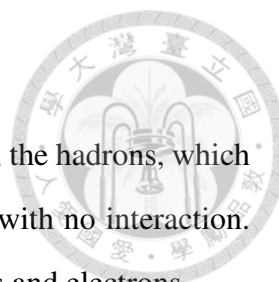


Figure 2.4: Structure of the ECAL [2]





### 2.4.5 Hadronic calorimeter (HCAL)

In ECAL, only photons and electrons can be fully captured. However, the hadrons, which are made of quarks and gluons, and muons can pass through easily with no interaction. So the HCAL is designed to measure the rest particles beside photons and electrons.

The schematic plot for the HCAL is shown in Figure 2.5. The HCAL can be separated into four parts. The HCAL barrel part (HB) and outer barrel part (HO) cover  $|\eta| < 1.6$ , the HCAL end-cap part (HE) covers  $1.5 < |\eta| < 3.0$  and the forward calorimeter (HF) covers  $3.0 < |\eta| < 5.2$ .

The HCAL is designed as a sampling calorimeter. In the HCAL, steel and brass are used as absorber and scintillator layer as readout layer. The steel plates are placed at very front and back and support the structure. There are 14 layers of brass plates are placed in between.

The effective thickness of the HB part increases with the polar angle ( $\theta$ ) as a function  $1/\sin\theta$ . At  $|\eta| = 1.3$ , the effective thickness comes to  $10.6\lambda_I$ , and it is around  $10\lambda_I$  in the HE part combine with the EE.

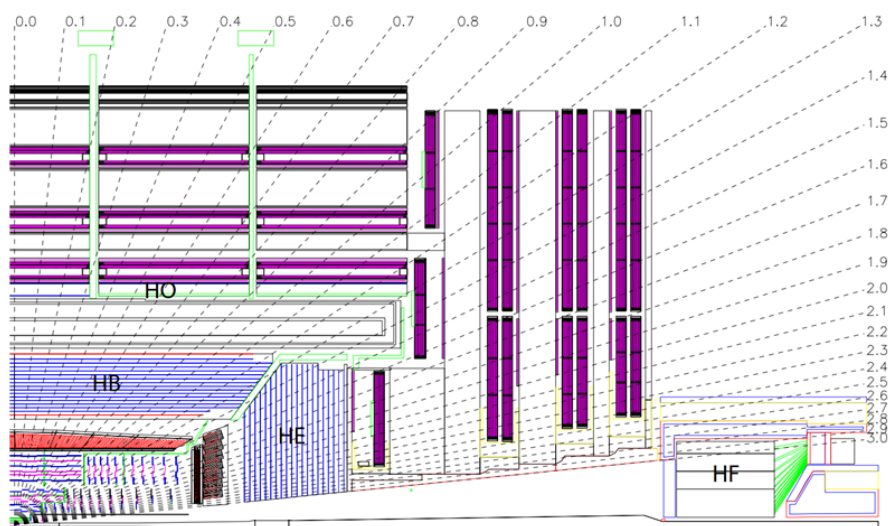
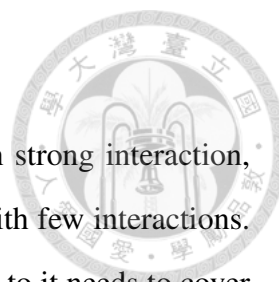


Figure 2.5: Structure of the HCAL [2]



### 2.4.6 Muon detector

Because muons have relatively higher mass and don't participate in strong interaction, muon can penetrate several meter of absorber (ECAL and HCAL) with few interactions. Thus, muon detector is placed in the outermost part in the CMS. Due to it needs to cover quiet large area, the ideal design for muon detector is gaseous detector. The operating principle for muon system in the CMS is that a pair of anode and cathode maintained at high voltage difference, the space in between is filled with inert gas, which is a mixture of argon and carbon dioxide. The gas would be ionized when muon passing through and the ions drifting toward the anode and cathode produces a measurable current. The schematic plot of muon detector is shown in Figure 2.6.

There three main detectors in the muon sub-system. The barrel drift tube part (DT), the cathode strip chambers (CSC) and the resistive plate chambers (RPC). The drift tube part covers the region  $|\eta| < 1.2$ . The CSC part locates at the end-cap region, covers  $0.9 < |\eta| < 2.4$ . The cathode strip chambers are designed as 2D array with anode wires and cathode strips which are perpendicular with each other for faster measurement. The RPC part covers  $|\eta| < 1.6$ , provides an independent measurement from DT and CSC part.

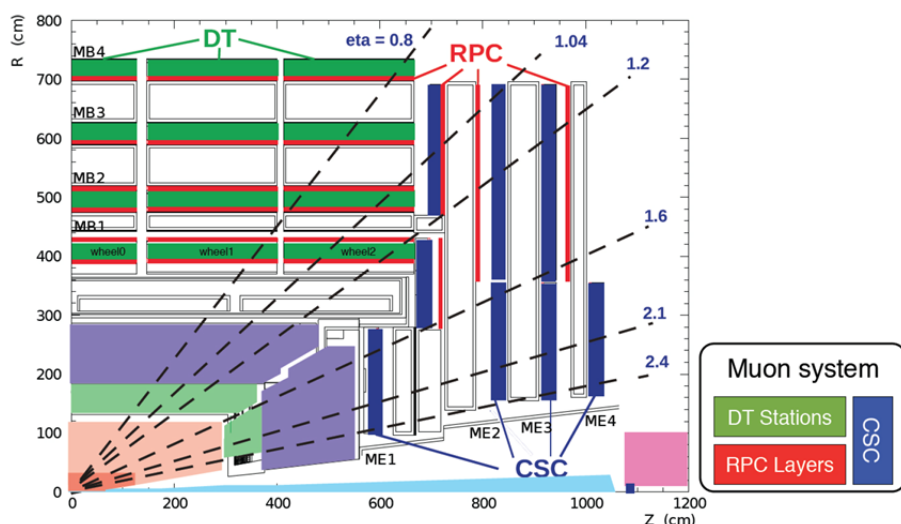
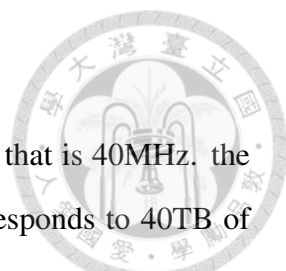


Figure 2.6: Structure of the Muon Detector [3]



## 2.4.7 Trigger system

As mentioned previously, the LHC beam crossing occur every 25ns, that is 40MHz. the recording of each detector responses takes about 1MB of data, corresponds to 40TB of data per second. It is impossible to store all the data, so the Trigger system is designed to select the events. There are two steps in the Trigger system, the Level-1 trigger (L1) and the High-Level Trigger (HLT), they select out all the detector readout only with the events that have specific signatures, and reduce the data size. The L1 trigger reduce the event rate to 30kHz and the HLT further reduce the rate down to minimum 100Hz.

The L1 trigger is comprised of programmable electronics, there local, regional and global components, shown in Figure 2.7.

The HLT is a software system, which is a farm consists of 1,000 computers. There are many algorithms in the HLT that can select for reconstruction physics events, thus the operating rate of the HLT is 100 ~ 20,000Hz.

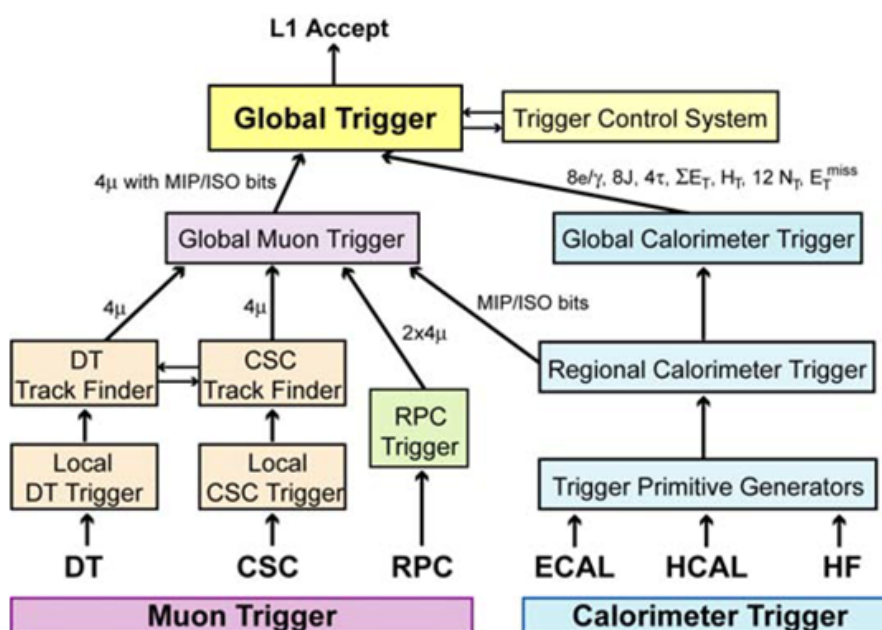
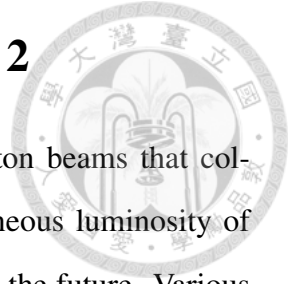


Figure 2.7: Architecture of CMS level 1 (L1) trigger system. [2]

### 3 The HGCal upgrade for the CMS phase 2



As mentioned in last chapter, the LHC currently produces the proton beams that collide with a center-of-mass energy of 13 TeV with average instantaneous luminosity of  $1.7 \times 10^{34} \text{ cm}^{-2}\text{s}^{-1}$  (2018). However, it will no longer be this case in the future. Various of upgrades has been taken in the LHC to improve the collision center-of- mass energy and to raise the luminosity from early stage. The history of the LHC operation as well as future target is shown in Figure 3.1.

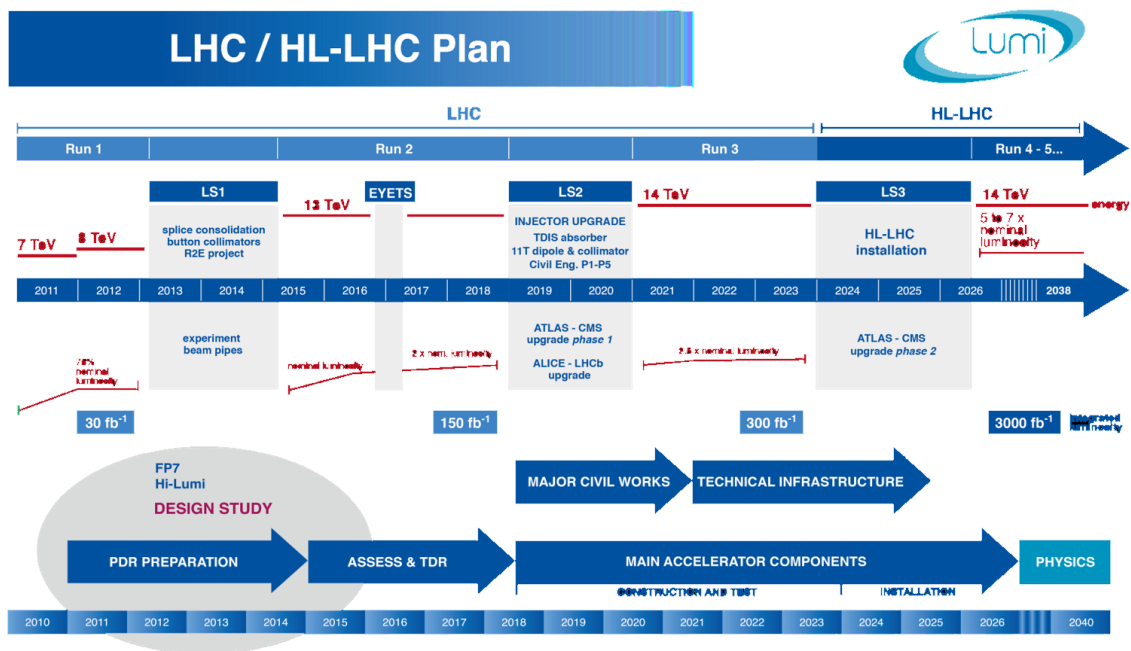


Figure 3.1: LHC upgrading schedule. [4]

By the end of 2018, the LHC has its second shutdown (LS2) to further raise the energy up to 14TeV. At the same time, the experiments in the LHC, include the CMS, will also upgrade the detectors. In the LS2, also called phase-1, upgrading will let all apparatus can cope with the conditions in the Run3. The overview of phase-1 upgrading for the CMS experiment can be found in [9].

The next upgrade for the LHC will be taken in the third long shutdown (LS3), which will take place in 2024~2026. In the LS3, the luminosity of LHC will be raised up to

$5 \times 10^{34} \text{cm}^{-2} \text{s}^{-1}$ . The LS3 upgrading will open a new era of operation in the LHC, the phase 2 operation, or so called high-luminosity LHC (HL-LHC).

The rising of the luminosity will definitely bring challenge to the whole experiment, including the radiation damage to the detectors and the electronics on detector and the high pileup condition. Furthermore, the integrated luminosity in HL-LHC is ten times more than the current LHC, which will degrade the performance of the ECAL and HCAL to an unacceptable level. Therefore, the replacement of the CMS calorimeters is inevitable and will take place in the LS3. The high-granularity calorimeter (HGCAL) is the most ideal technology for replacement of the end-cap part of the calorimeter.

HGCAL is designed to be sampling calorimeter in both EM and hadronic section. A large percentage of HGCAL will use silicon as the material of active layer, and the scintillator with direct SiPM readout will be used in the rest of calorimeter.

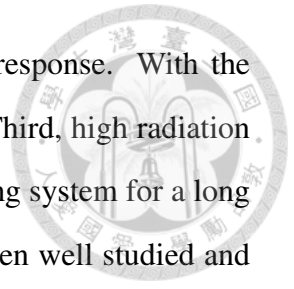
### **3.1 Silicon as active material in a sampling calorimeter**

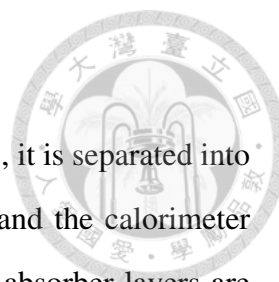
Since 1950's, the semiconductor has been used in particle physic. [10] Silicon is very ideal material to use for designing particle tracker, which requires high position resolution.

The working principle of silicon particle detector is quite different from crystalline material. To create a depletion area in doped silicon, a bias voltage is applied to remove all free charges in the region. As the voltage goes higher, the efficiency of charge collecting of silicon increase as well until it reaches a limit in which the full depletion is achieved. In addition, the thickness of the depletion area also strongly correlates to the charge collecting efficiency of the silicon. Practically, a voltage higher than the full-deplete voltage will be applied to the silicon and creates a stable electric field for charge collecting. When charged particle passes through the silicon leads to ionization and create electron-hole pairs, which are then collected by the electric field.

There are several advantages of silicon serves as active material. First, high energy resolution. The average energy required to produce an electron-hole pair is much smaller

than the energy to ionize gas in gaseous detector. Second, faster response. With the electron-hole pair, it only takes few nanoseconds to collect charge. Third, high radiation tolerance. In plenty of experiments, silicon has been served as tracking system for a long time, the efficiency drop of the silicon after radiation damage has been well studied and considered to be endurable in a such high radiation environment in the HL-LHC.





### 3.2 Overview of HGAL

The HGAL served as the new end-cap part calorimeter for the CMS, it is separated into two parts, the calorimeter end-cap electromagnetic section (CE-E) and the calorimeter end-cap hadronic section (CE-H). The material in active layers and absorber layers are different between the CE-E and CE-H.

The CE-E part of HGAL is composed of 28 layer longitudinal samplings and 24 layer for CE-H part. The cell size of silicon is about  $\sim 0.51\text{cm}^2$ . This high granularity will promote the accuracy of feature extraction and measurement of particle track of shower and jets.

The HGAL in the CMS will cover the region from  $1.5 < |\eta| < 3.0$ . The whole HGAL system will be cooled by a  $\text{CO}_2$  system to maintain the temperature at  $-30^\circ\text{C}$  to make sure the electronic noise, which results from the increasing leakage current, and the lose of efficiency of charge collecting stay in a acceptable range after irradiation. The schematic plots of HGAL are shown in Figure3.2.

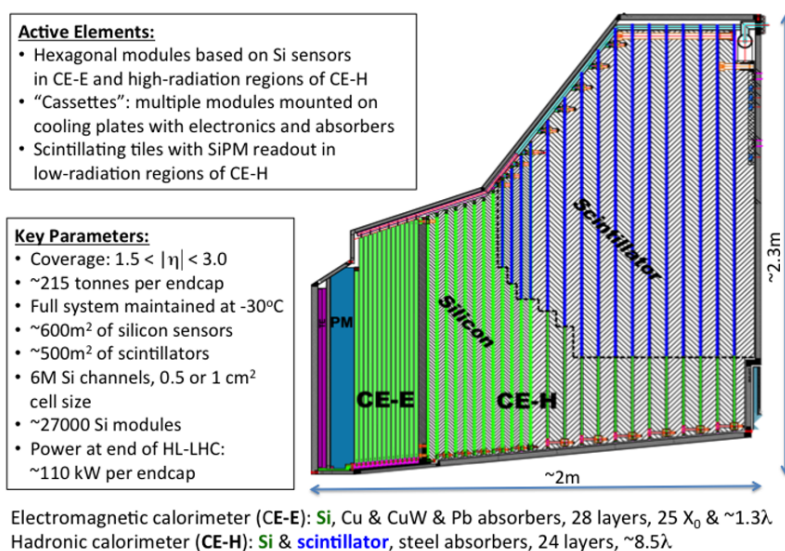


Figure 3.2: Material design for HGAL. [5]

To endure such high level of radiation in HL-LHC, the HGAL is designed as combination of silicon and scintillator base calorimeter. In high radiation region, silicon is used as absorber and in the low radiation region, the scintillator with SiPM readout is used.

In the CE-E part, there are 28 sampling layers contain in 30cm. Silicon sensors are attached on either side of a copper plate, and 14 copper support plates are inter-spaced by lead absorber. The total thickness of EE part is approximately  $25X_0$  for radiation length and  $1\lambda$  for interaction.

The CE-H part is about 1.5 m in depth and composed of 12 sampling layers in both the FH and BH sections, use stainless steel as the absorber. The thickness is  $3.5\lambda$  in FH section and  $5.7\lambda$  in BH, result in a total  $9\lambda$  for the 24 layers.



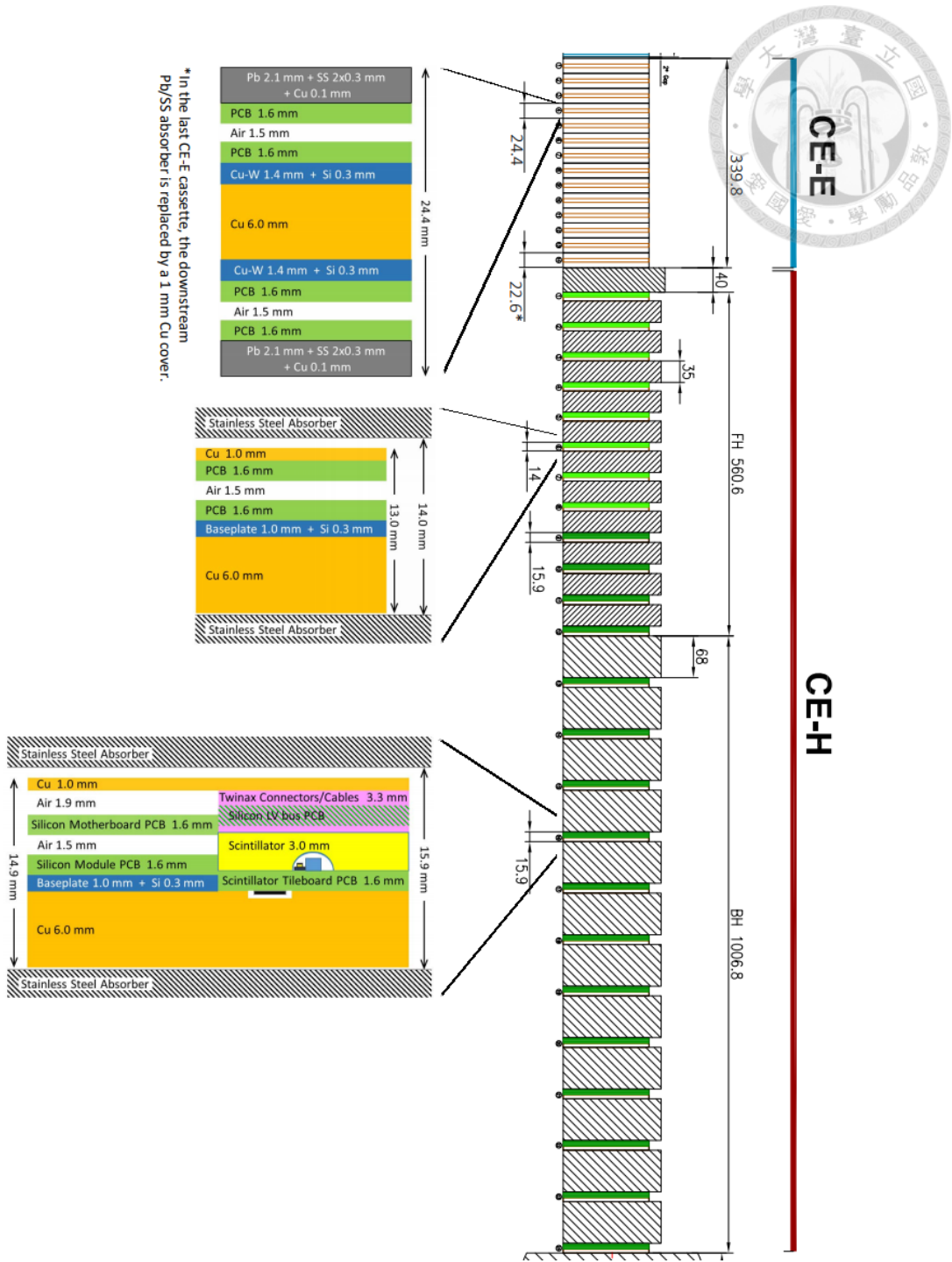


Figure 3.3: Longitudinal structure of the HGCal.

## 4 HGCAL beam-test prototypes

### 4.1 HGCAL modules

A single CE-E module design is composed of 4 parts, which are shown in Figure 4.1. The basic function of the 4 components are:

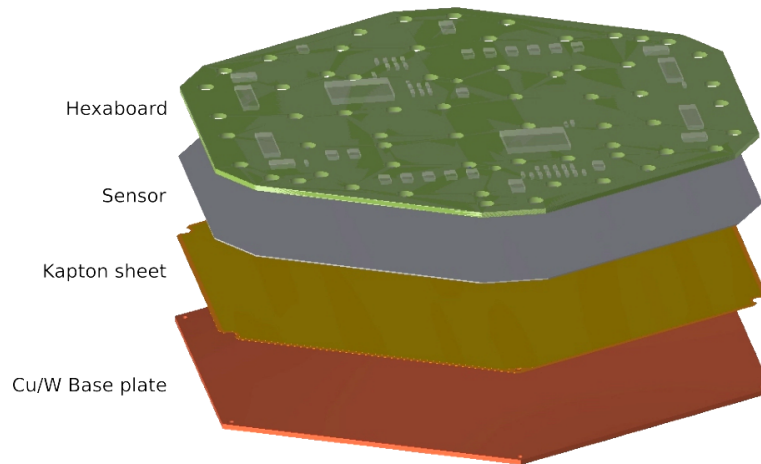


Figure 4.1: CE-E silicon module, showing stacked layers. [6]

- Printed circuit board (PCB): The PCB part is where the readout chips and the FPGA mounted. There are many holes on the PCB, aluminium wire bonds through the holes to the silicon sensor under the PCB, so the analog signal collected from the sensor can be routed to the readout chips and digitized.
- Silicon sensor: The diameter of silicon sensor is 6 inch. There are 133 or 134 hexagonal cells in the sensor, each with  $\sim 1$ cm in diameter. According to the shape of the cells, they can be classified into 4 types, which are inner/outer calibration cell, mouse bite, full hexagonal cell and half cell. Shown in Figure 4.2. Some of the cells are difficult to bond, so these cells are "merged" to the nearby cell which means they share the same readout. Non-complete hexagonal cells around the edge are also specially treated, to match the final 127 channels in the readout chain.
- Kapton sheet: A gold-surfaced sheet to allow biasing of the back side of the silicon

sensor while also served as an insulation between sensor and the base plate.

- Base plate: The base plate has 3 in 1 function in the test beam. First, it serves as support unit, provides mechanical rigidity to the module and prevent the fragile silicon sensor from bending. Second, it is the thermal path between the PCB and the cooling plate, which lead the heat produced from the elements, like chips and FPGAs, out of PCB. The last function is that it also serves as an absorber in the beam.

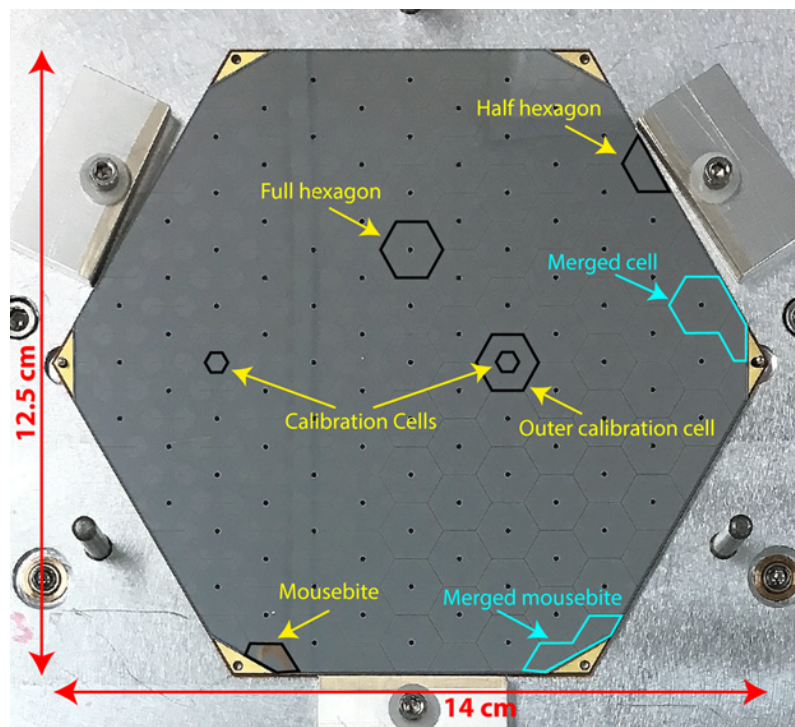


Figure 4.2: Sensor design. [5]

This picture shows the dimension of the silicon sensor and different cell types are labeled. Although the inner calibration cell is not always existing, the sensor layout stays the same in all the beam tests. The thickness of the active layer is different from 2016 to 2017/2018.

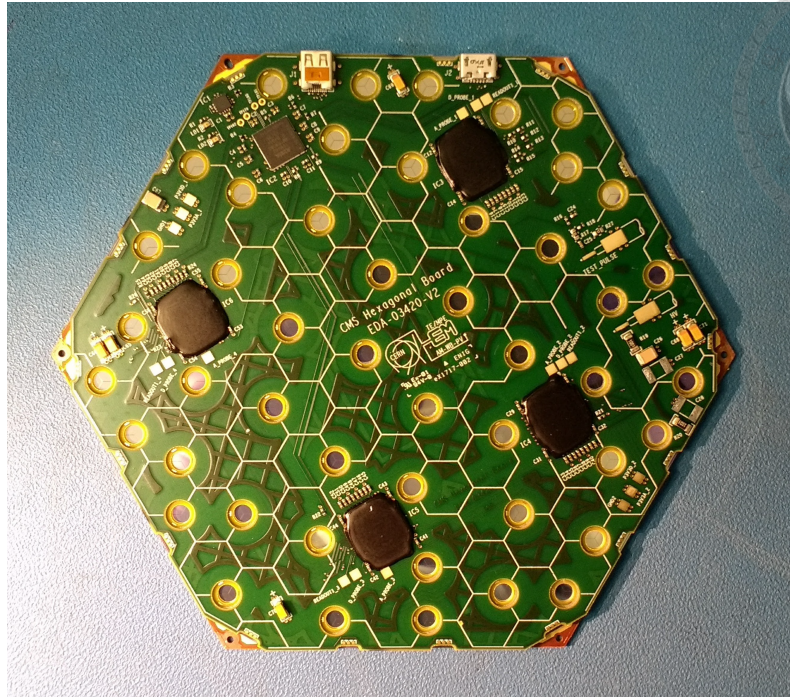


Figure 4.3: The complete module of the 2017/2018

In 2017/2018, different materials are used in the base plate including pure copper base plate, PCB base plate, copper with kapton and the copper-tungsten. With different material base plate, multiple tests related to the noise can be performed. Most of the base plate are 1.2 mm and some with special design are 2.4 mm. The mouse bite cell which made by joining two half-cells are no longer fully readout, which means only one of them is readout. The total channels in the readout chain remains 127. The PCB design is single layer PCB, which can collect the signal from the wire bond and directly transmit the analog signal to the front-end electronics on the same PCB. There are 4 ASICs (chips) used on the PCB, each of them response for 32 sensor cells.

## 4.2 2018 beam-test setup

The data were collected during October 2018 at the H2 beam line, [11], located in the EHN1 experimental hall of the CERN-SPS North Area. Secondary beams of hadrons or positrons up to a maximum momentum of 400 GeV/c can be transported in the experi-



mental areas with variable purity (10~99%). These secondary beams are produced by the interaction of the primary proton beam impinging on a thin beryllium plate primary target, designated 'T2'. The H2 beamline transports the produced particles over a length of approximately 600 m, with the last 250 m being inside the surface EHN1 experimental hall. The H2-beam line is a magnetic spectrometer consisting of dipole magnets, a number of quadrupoles and collimators. The H2 dipole spectrometer principle of operation is shown in Figure. 4.4.

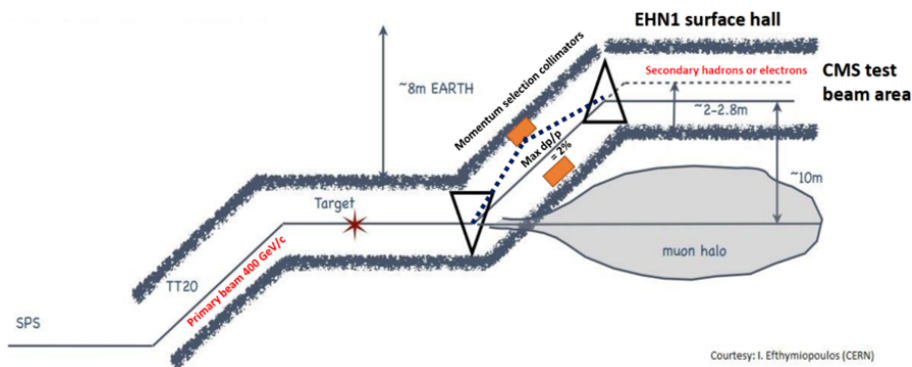


Figure 4.4: H2 beamline flexible magnetic spectrometer.

The primary beam from the SPS impinges on a Beryllium target and produces the secondary particles. They are subsequently momentum-analyzed and selected with the use of two series of vertical dipole magnets (depicted as triangles) and collimators depicted as orange rectangles.

The beamline selects the secondary particles produced at the target within a  $\Delta p / p = 0.2 \sim 2\%$  acceptance, depending on the upstream collimator settings. The currents of the first and second sets of dipoles define the beam momentum emerging from the last dipole of the spectrometer located 250 m upstream the HGAL prototype. The final beam is achromatic in first order, with a fixed momentum spread defined by the collimators. Optics-wise, only second-order chromatic aberrations introduce a negligible correlation between each particle momentum and its transverse position. For hadrons, this fixed momentum spread is the only contribution to the full spread of the beam energy.

However, for positrons, Synchrotron Radiation (SR) losses induce an additional beam spread that is particularly important for energies above 100 GeV. The total beam spread is given by the convolution of these two effects and is shown for positrons in Table 2. In the case of positrons, SR losses in the dipole magnets also lead to a final beam momentum that is lower than the nominal one.

| Nominal Momentum (GeV) | Final Momentum (GeV) |
|------------------------|----------------------|
| 20                     | 20.00                |
| 30                     | 30.00                |
| 50                     | 49.99                |
| 80                     | 79.93                |
| 100                    | 99.83                |
| 150                    | 149.14               |
| 200                    | 197.32               |
| 250                    | 243.61               |
| 300                    | 287.18               |

Table 2: H2 beamline positron beam momentum and momentum spreads.

The H2 beamline and HGCal-prototype experimental setup are shown in Fig. 4.5. The beamline section from the last spectrometer dipole to the face of the calorimeter, includes sections of air, beam windows and beam counters like delay wire chambers (DWC) and Cerenkov detectors accounting for about  $0.2X_0$  of material.

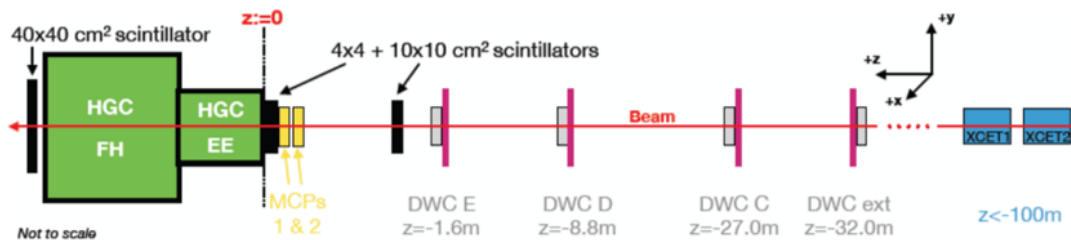


Figure 4.5: H2 beamline and HGCal-prototype experimental setup.

The DWC is most commonly used supporting detector in the HGCal beam tests at

H2 beam line. The DWC is built in an aluminium case of  $220 \times 220 \times 56$  (mm), with two kapton windows of  $110 \times 110$  (mm) and a thickness of  $25 \mu\text{m}$ . The picture of DWC is shown in Figure 4.6

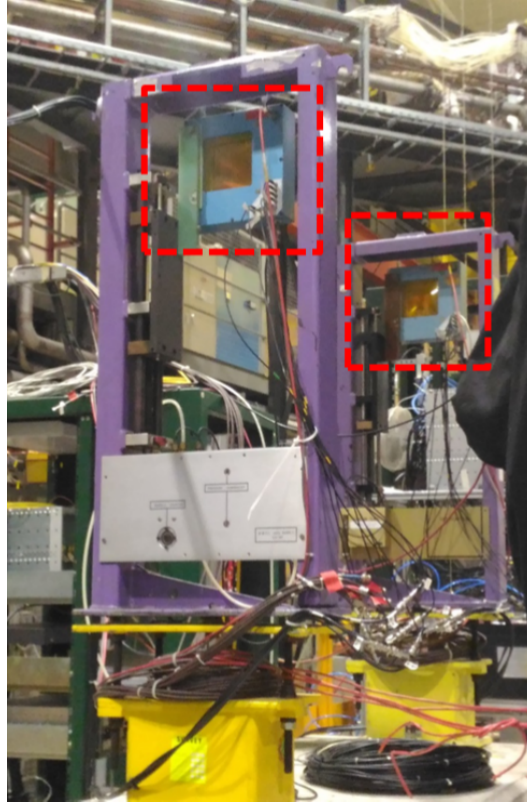


Figure 4.6: Delay wire chamber and supporting frame.

The supporting frame and the DWC is shown. The functioning part is labeled by the red frame.

The DWC is a gaseous detector, when a particle passes through, the ionized gas will be accelerated by the high voltage between the thin cathode and anodes. The DWC has 4 direction TDC(time to digital converter) readouts (top, bottom, left and right), by calculating the delay between x or y, the point where the particle penetrates is retrieved. By using multiple DWCs in the beam line, the track of the particle can be reconstructed. The extrapolation of this track to the HGCAL prototype can serve as a reference for studying position resolution as well as an event selection to reject the particle deviated from the

normal trajectory. The resolution of the DWC in the H2 beam line is 0.2 mm, which is enough for the cell size of the sensor ( $\sim 1\text{cm}$ ).



#### 4.2.1 HGICAL Prototype

The HGICAL prototype tested in October 2018 comprised a CE-E and a CE-H section. The CE-E section consisted of 28 sampling layers of hexagonal modules with hexagonal Si pads ( $\approx 1\text{ cm}^2$ ) interleaved with alternating copper plus copper-tungsten absorbers or lead plus stainless steel absorbers. For the 2018 beam test, 28 hexagonal modules were assembled from a stack of a copper-tungsten baseplate, a polyimide foil, a silicon sensor and a readout PCB (referred to as Hexaboard).

The modules followed the same design as the prototypes tested in 2016, albeit with better grounding to improve the electronic noise and take advantage of the new Skiroc2-CMS front end chip [12]. The Skiroc2-CMS ASIC was specifically designed for HGICAL requirements. It offered a broad range of energy measurement thanks to a dual-gain amplification and an additional time-over-threshold technique (TOT) to cope with very high energy deposits where the low gain channel saturates. For the low and high gain chain, signal pulses collected from each Si pad were amplified, shaped, sampled with a 25n sampling frequency and finally stored in a 13 Switch Capacitor Array rolling analog memory (SCA). The chip also provided a time-of-arrival measurement (TOA) to allow shower time development studies. These changes aimed to get closer to the HGICAL ultimate performance and validate the simulation on which all high level analyses rely on.

The prototype tested in 2018 offered a variety of three configurations, among which the two first had identical CE-E section of 28 instrumented layers, close to the HGICAL design. The layout of the CE-E section is shown in Fig. 4.7. The results presented in this work were based on the data taken with these two configurations. Complete description of the prototype tested in 2018 CERN beam tests can be found in [13], including the CE-H section.





Figure 4.7: Layout for the CE-E prototype.

The CE-E prototype is built of 14 cassettes, where one cassette carries two hexagonal modules. In a hexagonal module, the Si sensor (dark blue) is located between the copper-tungsten plate and the Hexaboard. A cassette starts with a lead plus stainless steel absorber (light blue and pink) and ends with the Hexaboard (green) of the second module. The lead plus stainless steel absorber of the second cassette is also shown.

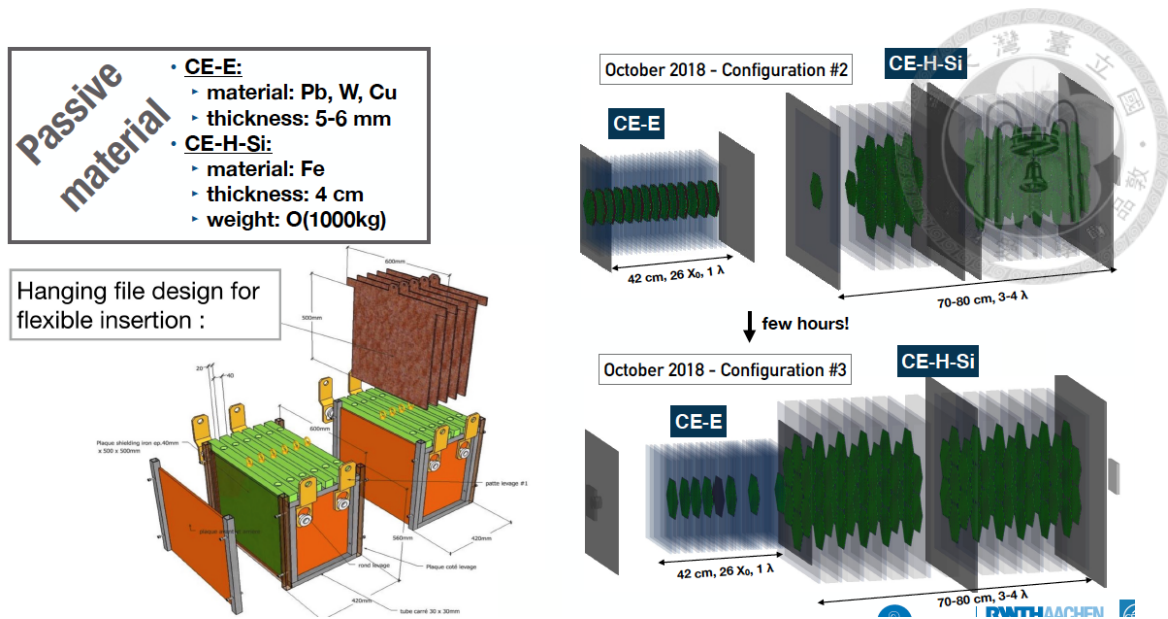


Figure 4.8: Test beam CE-E and CE-H setup.

#### 4.2.2 Trigger and DAQ systems

The Data AcQuisition system [5] consisted of DAQ crates with back-end components and a DAQ computer. Seven Hexaboards were connected via seven interposer boards to the readout cards. The latter were controlled by a Synchronising board delivering a 40 MHz clock, TTL Trigger and busy signals. The readout cards and the synchronising board were hosted in the DAQ crates. For the CE-E prototype, four readout cards were used to read the 28 layers. The DAQ computer running the EUDAQ software [14] collected the data from the readout cards as well as the data from the complementary beam detectors via a Gigabit Ethernet server. Scintillators were used to trigger the acquisition. A low-level electron trigger was obtained online, requiring the coincidence of 2 scintillators upstream the CE-E prototype and the veto of a scintillator downstream the CE-H prototype.

## 5 Electron energy reconstruction



To reconstruct the energy that deposited by showering electron in the CE-E, there are three necessary steps:

- The energy deposited in each Si active layer, which is noted as  $E_i^{Si}$ , where  $i$  is the layer number.
- The predicted energy deposited in an absorber layer  $E_i^{Abs}$  is added to the active layer energy to obtain the total energy deposited in CE-E. The prediction is based on layer weight, which is noted as  $W_i$ , applied to the active layer energy  $E_i^{Si}$ .
- The energy losses should be estimated and add to reconstruct the energy. The upstream losses  $E_{Up}$ , the lateral losses  $E_{Lat}$  and the longitudinal losses from energy leaking from the back  $E_{Leak}$ .

$$E_e = \sum_i^{N_{layer}} (W_i \times E_i^{Si}) + E_{Up} + E_{Lat} + E_{Leak} \quad 5.1$$

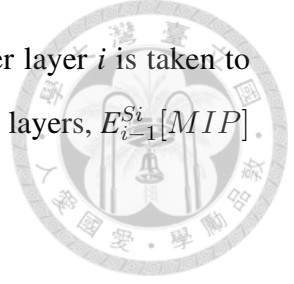
### 5.1 The dEdx method

The conventional method to rebuild the energy deposited in the absorber layers in silicon based sampling calorimeters, is to use the Most Probable Value (MPV) of the  $dE/dx$  distribution for a MIP in the absorber layer, which depends on the geometry of the absorber layers. In this method, the energy deposited in the absorber  $i$  is given by:

$$n_i^{Abs} \times \Delta E_i^{Abs} \quad 5.2$$

Where  $\Delta E_i^{Abs} = \frac{dE^{Abs}}{dx_i}(\text{MIP MPV}) \times \Delta x_i^{Abs}$  is the MPV of the  $dEdx$  distribution for a MIP in the absorber layer  $i$  and  $n_i^{Abs}$  represent the number of MIPs in the Si layer  $i$ . For the layer 1 we assume that one charged incident particle.

$$n_1^{Abs} = \frac{1 + E_1^{Si}[MIP]}{2} \quad 5.3$$



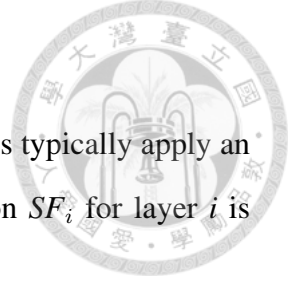
Except the layer 1, the number of MIPs passing through the absorber layer  $i$  is taken to be the average of the number of MIPs in the two nearby silicon active layers,  $E_{i-1}^{Si}[MIP]$  and  $E_i^{Si}[MIP]$ :

$$n_i^{Abs} = \frac{E_{i-1}^{Si}[MIP] + E_i^{Si}[MIP]}{2}, i = 2, \dots, 28 \quad 5.4$$

In a sampling configuration, combining Equation 4.3 and 4.4, we can get the estimation of the total energy  $E$  deposited in the passive and active layers in the calorimeter

$$\begin{aligned} E &= \frac{\Delta E_1^{Abs}}{2} + \sum_{i=1}^{27} \left( \frac{\Delta E_i^{Abs} + \Delta E_{i+1}^{Abs}}{2} + \Delta E_i^{Si} \right) \times E_i^{Si}[MIP] + \left( \frac{\Delta E_{28}^{Abs}}{2} + \Delta E_{28}^{Si} \right) \times \Delta E_{28}^{Si}[MIP] \\ &= \frac{\Delta E_1^{Abs}}{2} + \sum_{i=1}^{28} (W_i E_i^{Si}[MIP]), \end{aligned} \quad 5.5$$

where  $\Delta E_i^{Si} = \frac{dE^{Si}}{dx_i}(\text{MIP MPV}) \times \Delta x_i^{Si}$  is the MPV of the dEdx distribution for a MIP in the Si sensor  $i$ , which namely the factor that convert the Si sensor energy into MIP units. This approach works well when dealing with thin sampling absorbers which the ionization represents the main process of energy deposition.



## 5.2 The sampling fraction method

The sampling fraction method for calibrating sampling calorimeters is typically apply an inverted sampling fraction constant(SF), where the sampling fraction  $SF_i$  for layer  $i$  is defined as:

$$SF_i = \frac{E_i^{Si}}{E_i^{Si} + E_i^{Abs}} \quad 5.6$$

In practical, it is not realistic to calculate the SF for all 28 layers and all possible energies, a simplified way is take the average SF over the complete detector, providing a single weight for all layers as a function of the electron beam energy:

$$\langle SF \rangle = \frac{\sum_{i=1}^{28} (E_i^{Si})}{\sum_{i=1}^{28} (E_i^{Si} + E_i^{Abs})} \quad 5.7$$

There are two advantages of using SF. First, the relevance between the SF and energy is small, the SF barely changes with energy. Second, the SF can be estimated and parameterized using simulation. The reconstructed energy deposited in the complete detector can be written as:

$$E = \langle SF \rangle^{-1} \times E_{tot}^{Si} \quad 5.8$$

An advantage of using the energy dependent SF weights is the expected linearity and the consistent absolute energy scale in which the dEdx method does not provide the absolute energy deposited in the calorimeter. In the CMS, the lack of knowledge of the true energy can be corrected by interpolation after the initial guess of the full energy that given by the approximate SF weight. On the other hand, the disadvantage of sampling fraction method is that it is still not practical to calculate all the  $\langle SF \rangle$  for all energies and all pseudo-rapidities.



### 5.3 EM calorimeter energy resolution

For an ideal calorimeter, the intrinsic energy resolution is due to the fluctuation of total track length of shower  $T_0$ , which is proportional to

$$T_0 \propto E \quad 5.9$$

where  $E$  is the beam energy. Since  $T_0$  is proportional to the number of track segments in the shower and the shower development is a stochastic process, the intrinsic energy resolution is given by

$$\sigma(E) \propto \sqrt{T_0} \propto \sqrt{E} \quad 5.10$$

from which the well-known dependence of the fractional energy resolution

$$\frac{\sigma(E)}{E} \propto \frac{1}{\sqrt{E}} \quad 5.11$$

can be derived.

For the real calorimeter, the actual energy resolution is deteriorated by other contributions and can be written in a general form as

$$\frac{\sigma_E}{E} = \frac{S}{\sqrt{E}} \oplus \frac{N}{E} \oplus C \quad 5.12$$

Where  $\oplus$  is quadratic sum. The first term is called the 'stochastic term', the second term is the 'noise term'; and the last term is the 'constant term'.

### 5.4 Stochastic term

As mentioned previously, the stochastic term is due to the fluctuation related to the physical development of the shower, which is a stochastic process. Typical stochastic terms of homogeneous electromagnetic calorimeter are at the level of a few percent in units of  $1/\sqrt{E(\text{GeV})}$ . While in sampling calorimeter, the energy deposited in the active layers

fluctuates event by event because the active layers are inter leaved with absorber layers. These fluctuation, which are called 'sampling fluctuation' and the limitation to the energy resolution of the sampling calorimeter are due to the number of MIPs  $N_{MIP}$  which cross the active layers. This number is proportional to

$$N_{MIP} \propto \frac{E}{t} \quad 5.13$$

, where t refers to the thickness of the absorber layer. If the absorber layer is not too thin, then the sampling contribution to the energy resolution comes from the fluctuation of  $N_{MIP}$ , that is

$$\frac{\sigma}{E} \propto \frac{1}{\sqrt{N_{MIP}}} \propto \sqrt{\frac{t}{E}} \quad 5.14$$

The typical energy resolution of sampling EM calorimeter is in the range  $5\sim 20\%/\sqrt{E(\text{GeV})}$ . For the 2018 test beam HGCAL, the energy resolution is

$$\frac{\sigma}{E} = \frac{23\%}{\sqrt{E(\text{GeV})}} \quad 5.15$$

## 5.5 Electron energy reconstruction

The CE-E prototype was exposed to positron beams of nominal energies ranging from 20 to 300 GeV, in table 3 the beam energy, corresponding run number and the total events are listed. The distribution of reconstructed energy  $E_{visible}$  fit with Gaussian in both data and M, shown in Figure. 5.1. The red line is MC and the black line is data. In Figure. 5.2 the energy linearity and resolution are shown for the different energy reconstruction methods. It is important to show that this equation gives the correct scale for all energies when (i) all the losses are included and (ii) when the inverted average sampling fractions are used as weights. This is a form of closure test that is shown in Fig. 5.2 by open blue rectangles.



| Beam Energy (GeV) | Run number     | number of events |
|-------------------|----------------|------------------|
| 20                | 1012,1014,1015 | 30558            |
| 30                | 1008,1010,1011 | 31080            |
| 50                | 960,961,962    | 20302            |
| 80                | 971,972,973    | 39051            |
| 100               | 477,479,480    | 26163            |
| 150               | 493,494,495    | 31664            |
| 200               | 664,665,666    | 30845            |
| 250               | 652,653,654    | 29513            |
| 300               | 424,425,435    | 34028            |

Table 3: The beam energy and corresponding run number.

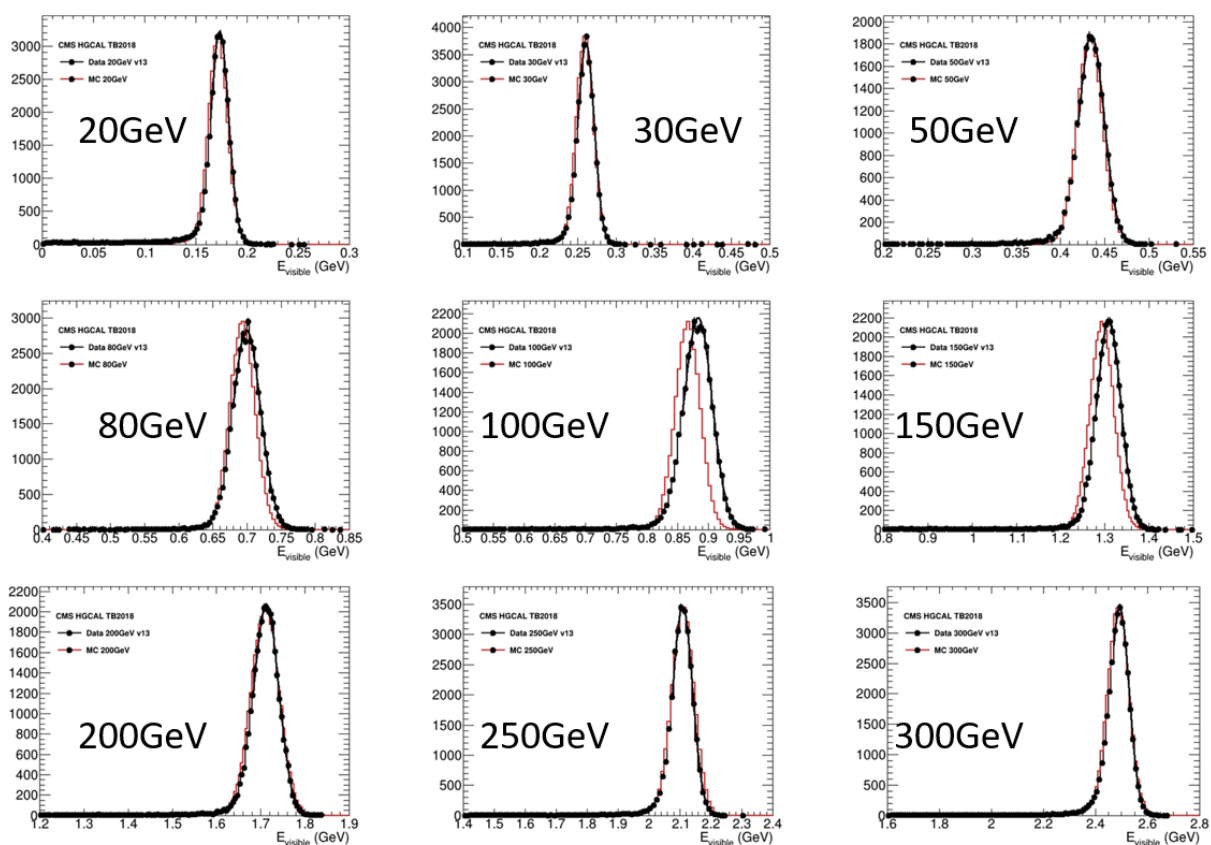


Figure 5.1: Reconstruction energy  $E_{rec}$  distribution.



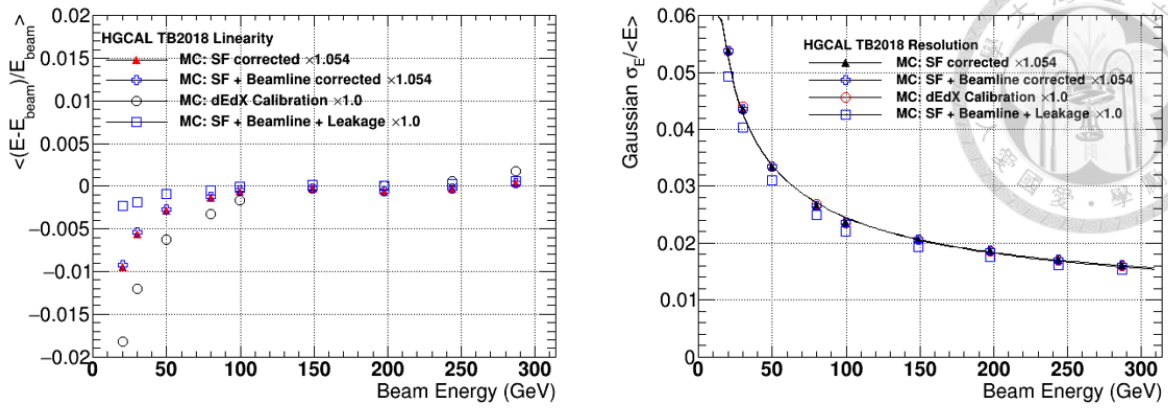


Figure 5.2: Energy linearity and resolution of MC.

Energy linearity (left) and resolution (right) for the dEdx method without addition of upstream, lateral and leakage from the back losses (black circles), the SF method without including losses (black triangles), the SF method including only upstream losses (crosses), and the SF method including all losses (blue rectangles). The obtained resolution without correction for losses leads to a stochastic term of  $22.91 \pm 0.07\%[\sqrt{\text{GeV}}]$  and a constant term of  $0.86 \pm 0.01\%$ . The loss of linearity is about 0.5% at very low energies. We can also see that the energy scale is recovered at high energies when considering all the factors of leakage.

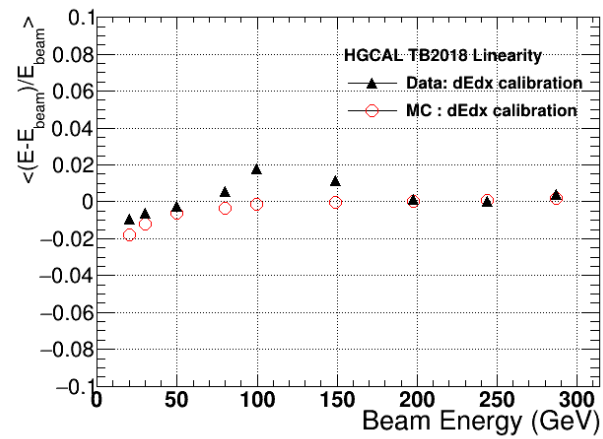


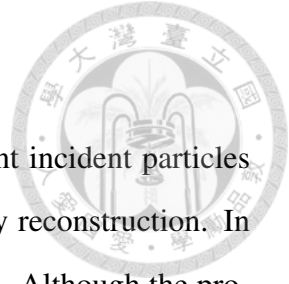
Figure 5.3: Linearity plot of Data and MC.

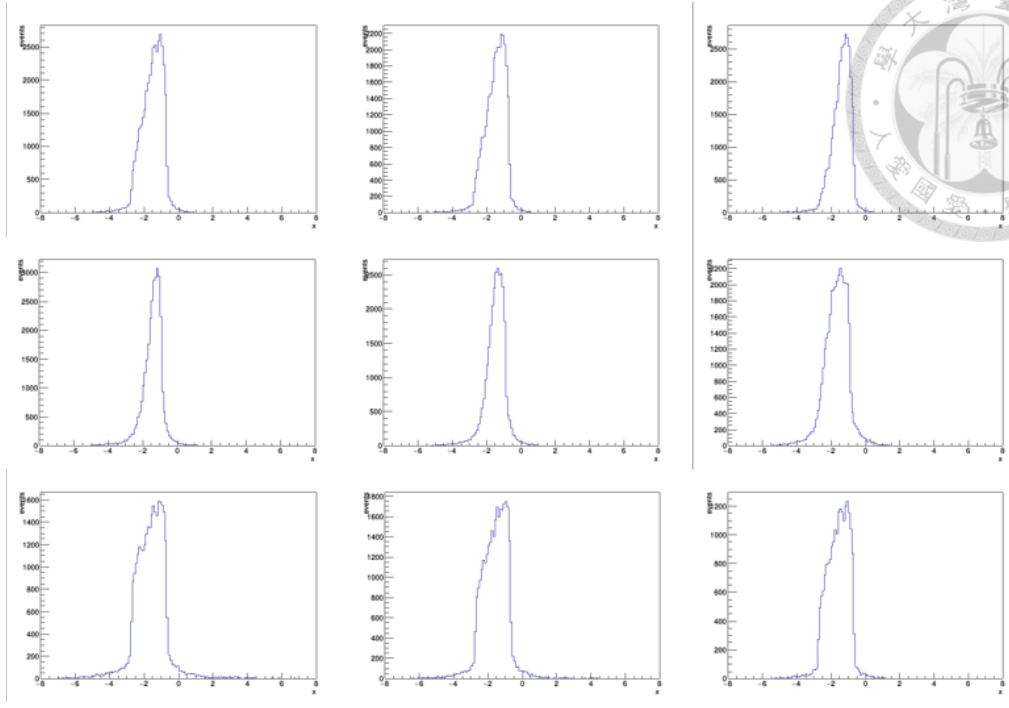
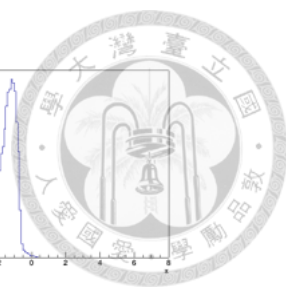
A 2% non linearity is observed in the data at low energy as we see in MC, thus the data and MC is basically in a good agreement. However, further studies are needed for 100GeV and 150GeV that show departure from expectation.

## 6 Uniformity Study

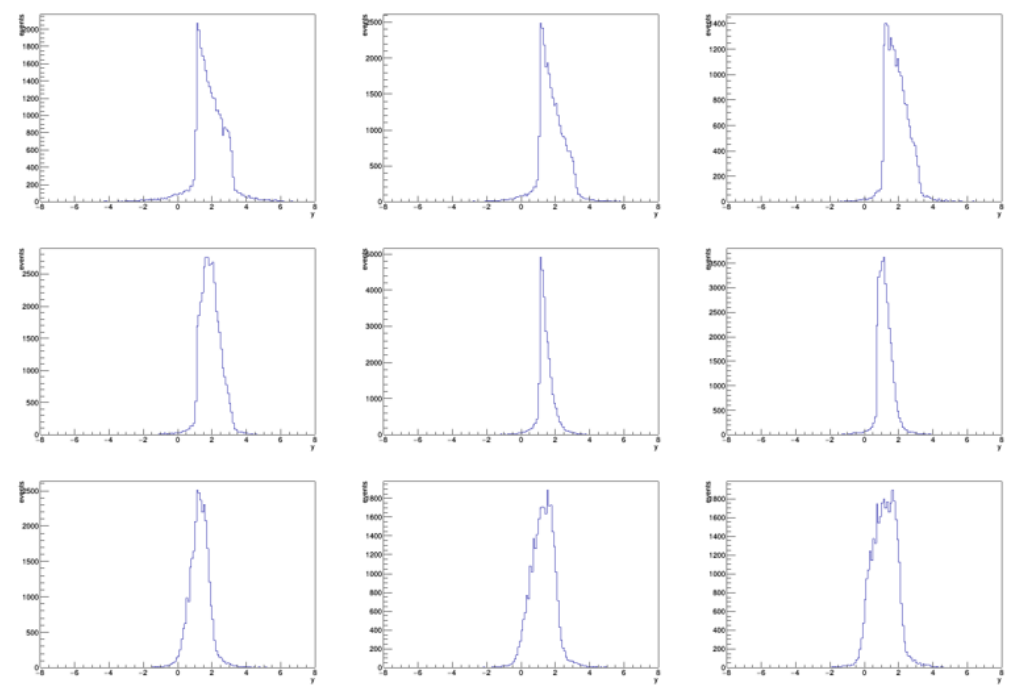
For a real module the material is not homogeneous, thus for different incident particles position, the module is expected to have different response in energy reconstruction. In this chapter we study the uniformity of the 2018 test beam prototype. Although the prototype in MC simulation is expected to be perfectly uniform, containment effects can also give non-uniformity. On the other hand, in the MC the electronic noise, cross talk, electronics calibration etc. are not simulated, which may cause a mismatch between data and MC. Such effects we would also like to study.

First, we need to separate the prototype acceptance in several areas. To do so, we need to check where the beam hits module. The number of events versus position distributions are shown in Figure 6.1. The prototype is separated into 8 regions-pads in both real data and MC. Each pad is a  $1 \times 1 \text{ cm}^2$  square to match the size of cell. In the data, the pads located at  $y: 0.5 \sim 2.5 \text{ cm}$  and  $x: -0.5 \sim 3.5 \text{ cm}$ , and in the MC, the pads locate at  $y: -1 \sim 1 \text{ cm}$  and  $x: -0.5 \sim 3.5 \text{ cm}$ . (Notice that in data, the  $x$  bin of pad 1 and pad 5 is actually  $x: -0.7 \sim 0.7 \text{ cm}$ , in order to get more statistic.) The  $E_{visible}$  distributions of different pads are shown in Figure. 6.4. In the data, most of events locate in the range  $x: 0 \sim 4, y: 0.5 \sim 3.5$ . In the MC, most of events locate in the range  $x: -0.5 \sim 3.5, y: -2 \sim 2$ .

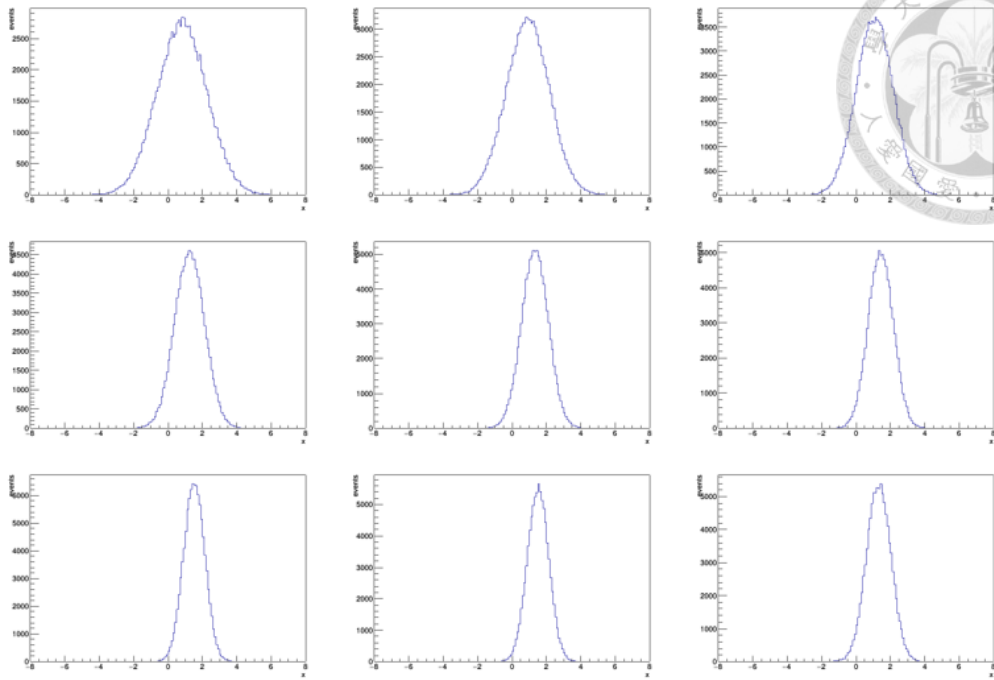




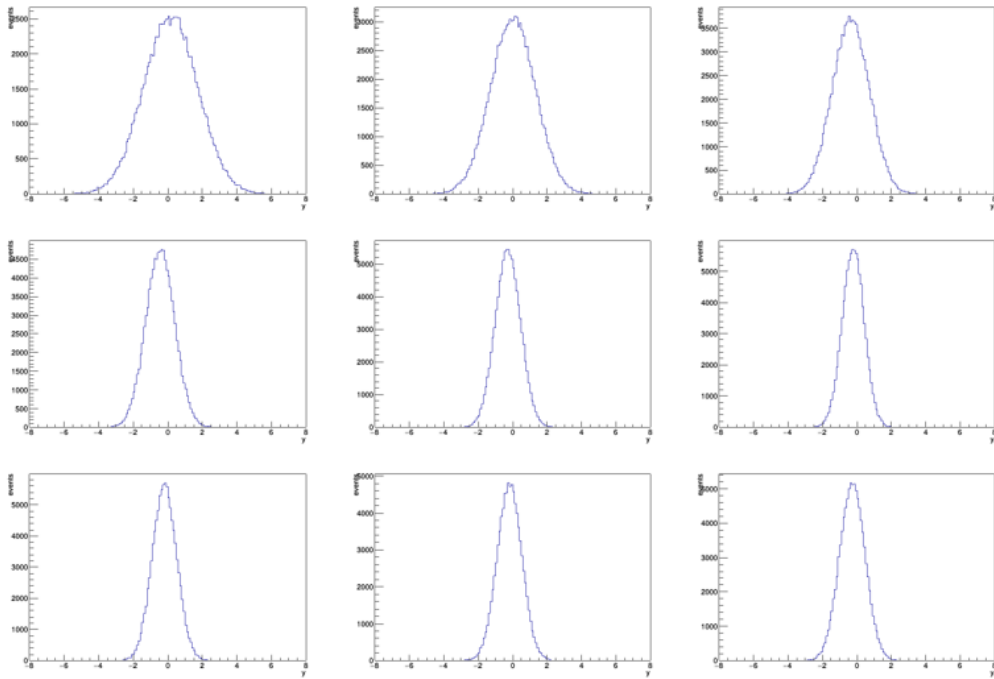
(a) x (Data)



(b) y (Data)



(c) x (MC)



(d) y (MC)

Figure 6.1: Distribution of event position.

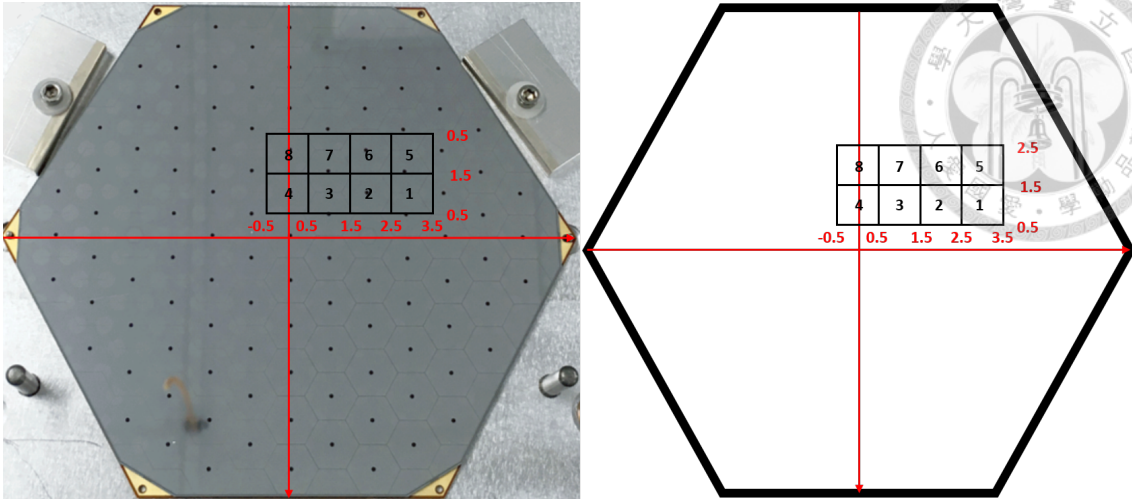


Figure 6.2: The schematic diagram of pad location and number on the module of data.

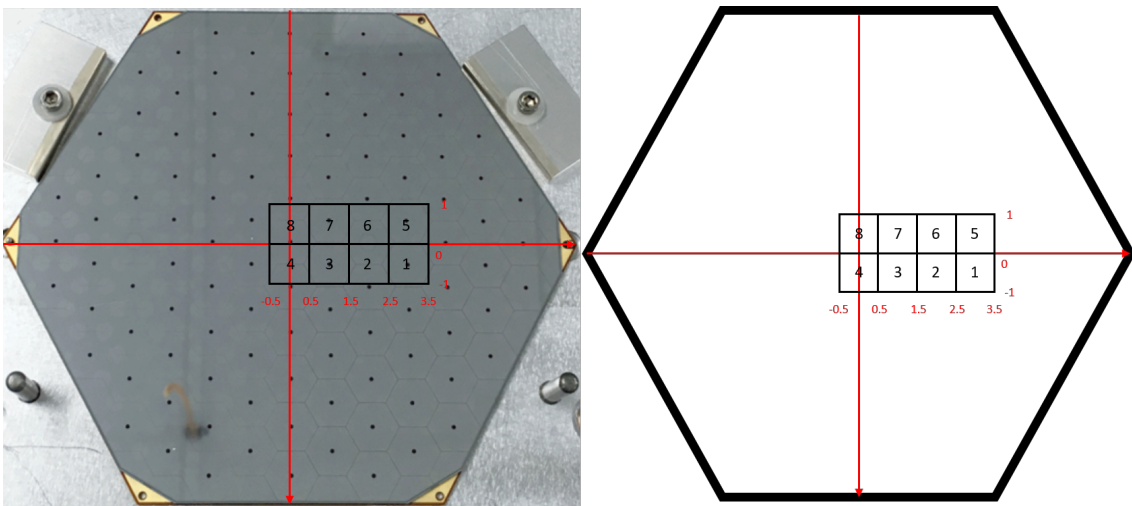
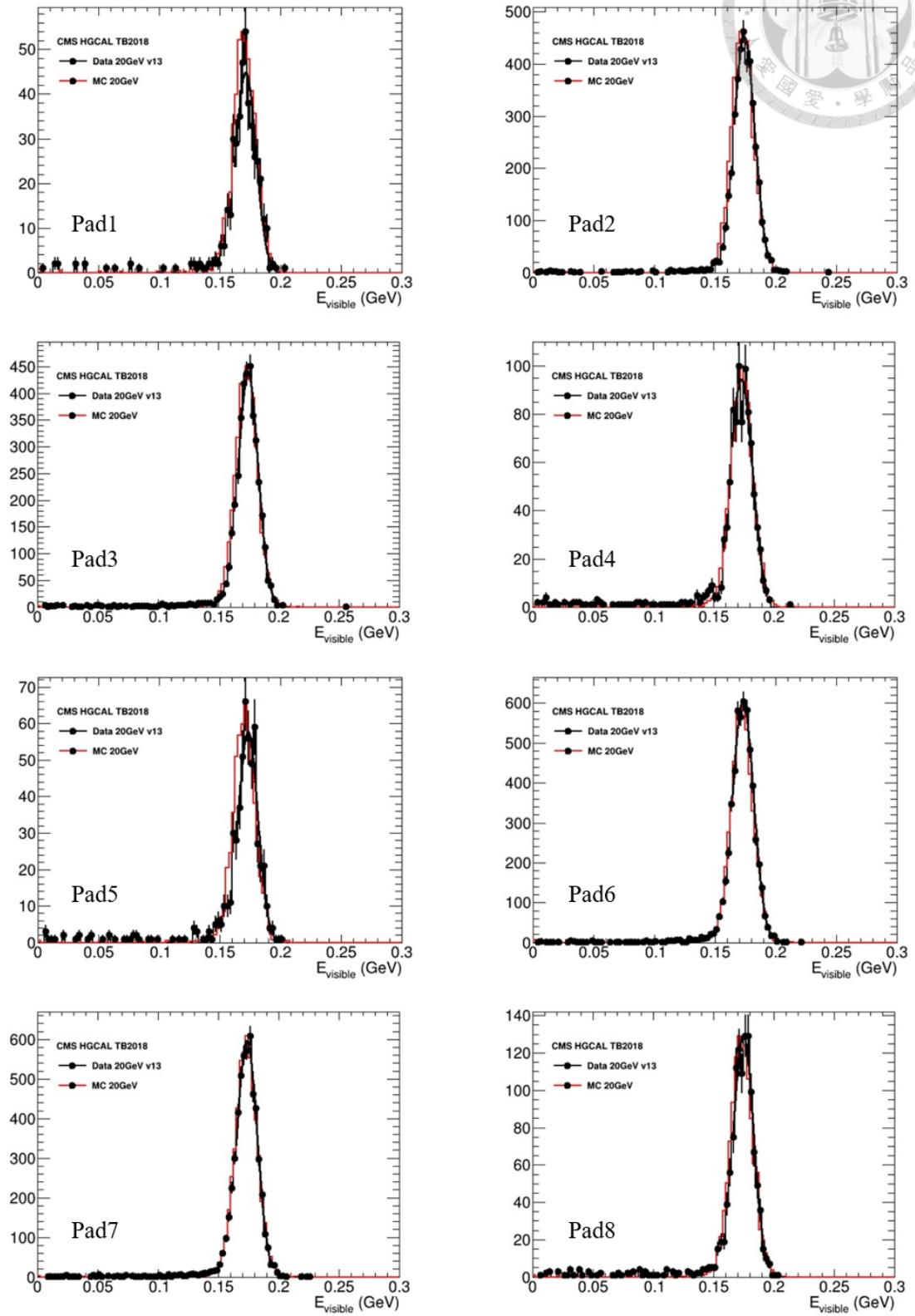
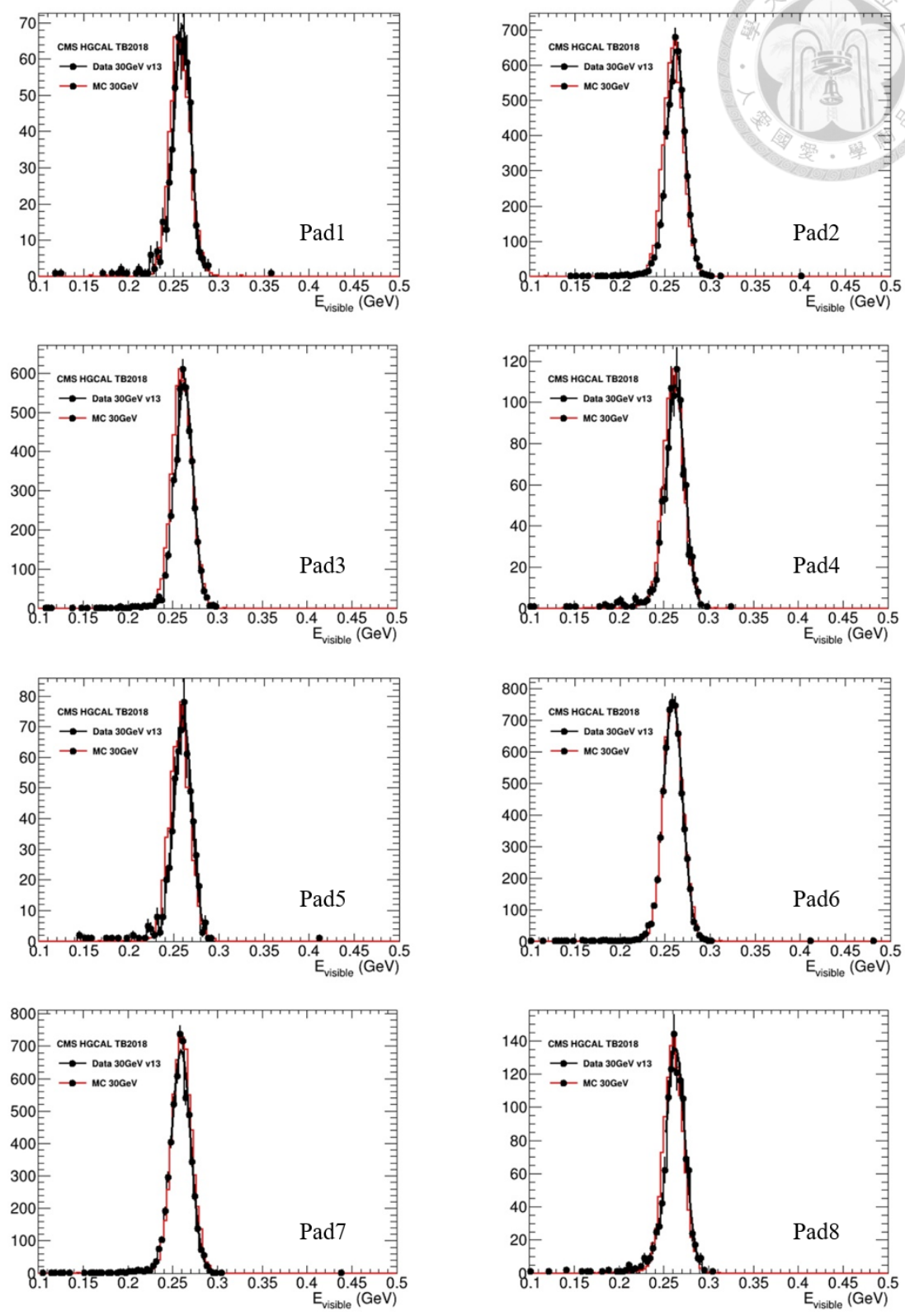


Figure 6.3: The schematic diagram of pad location and number on the module of MC.

Figure 6.4: The distribution of  $E_{\text{visible}}$  in different pads.

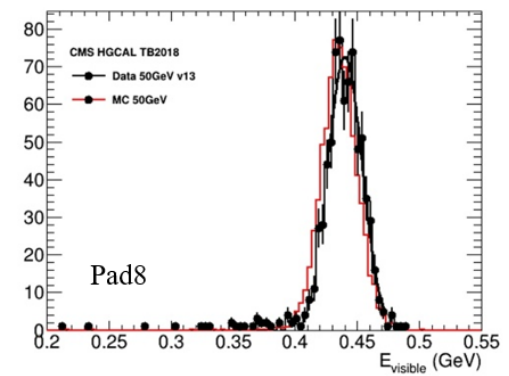
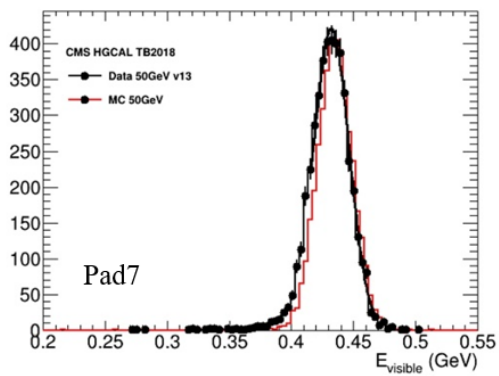
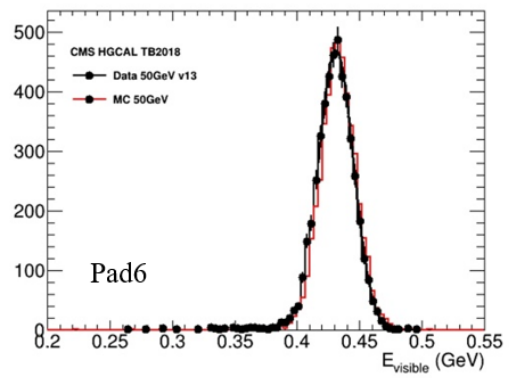
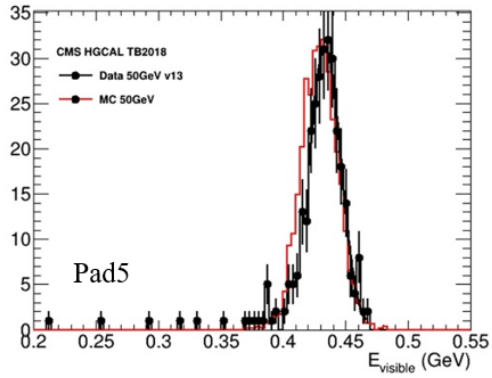
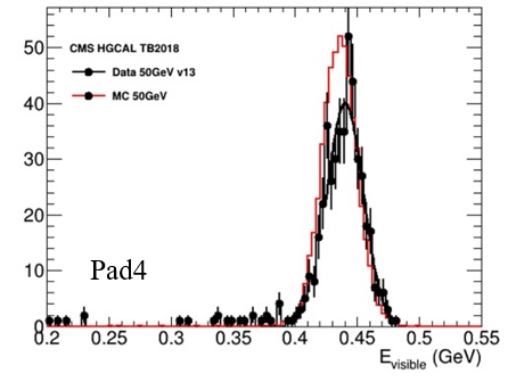
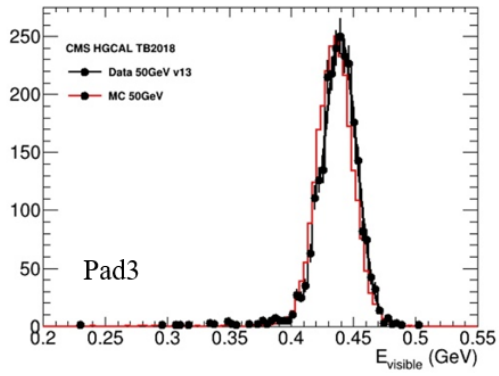
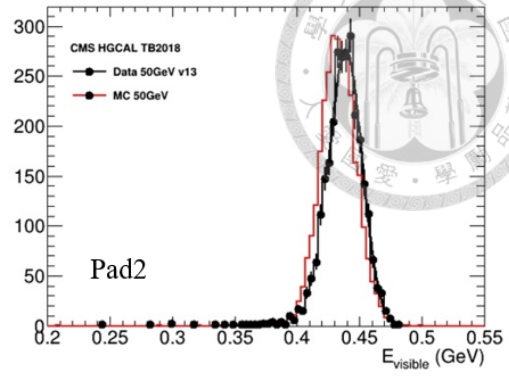
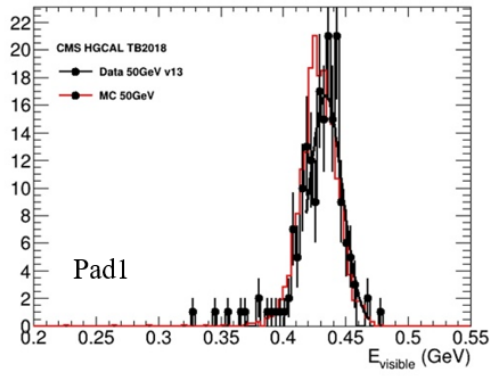


(a) 20GeV

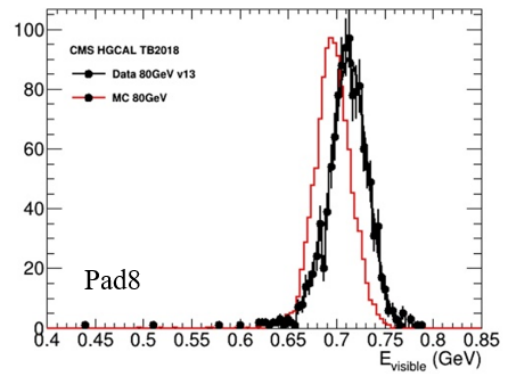
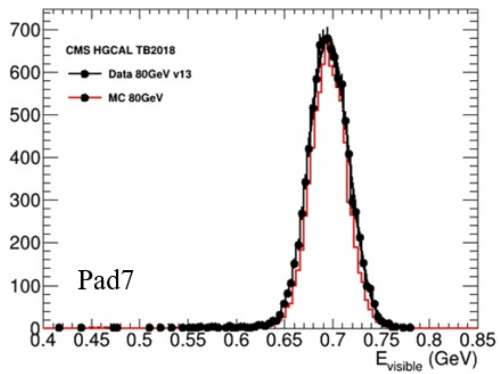
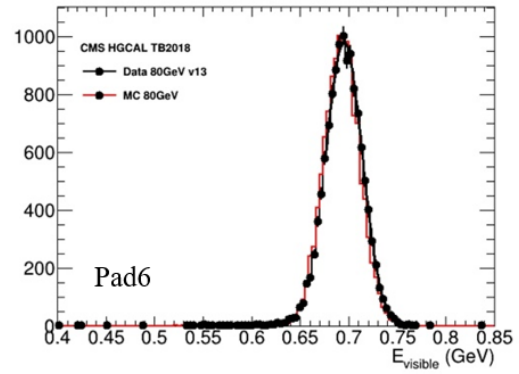
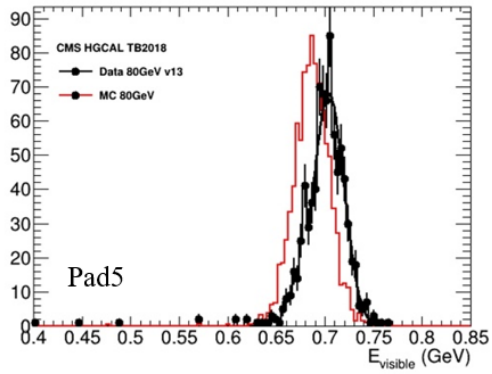
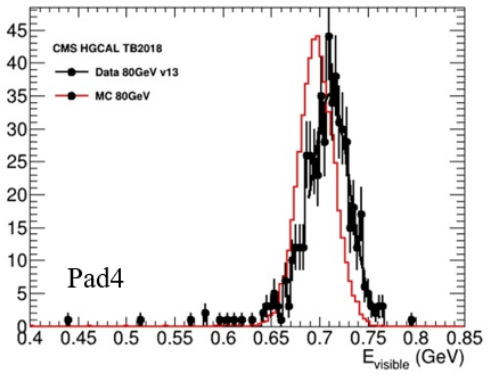
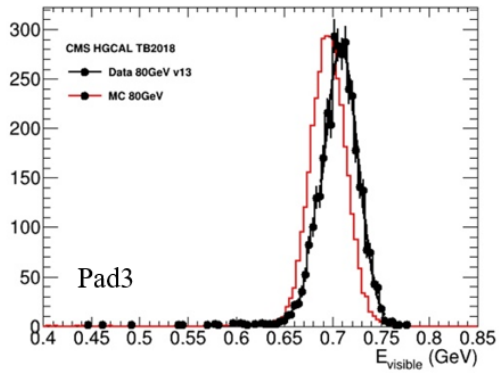
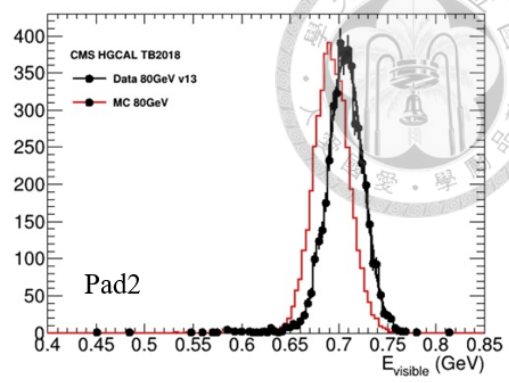
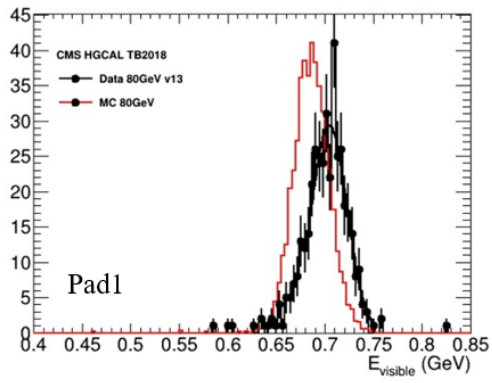


(b) 30GeV

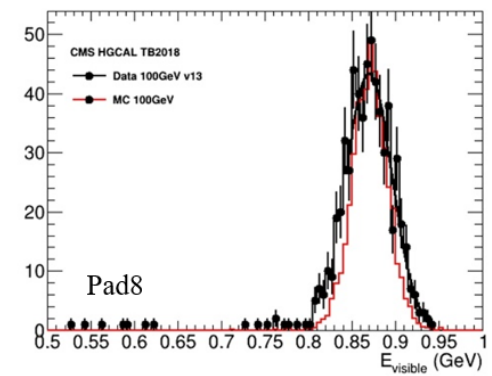
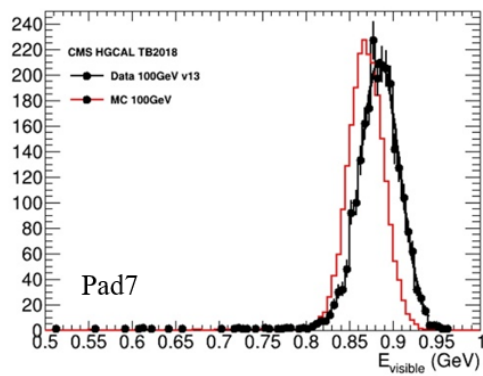
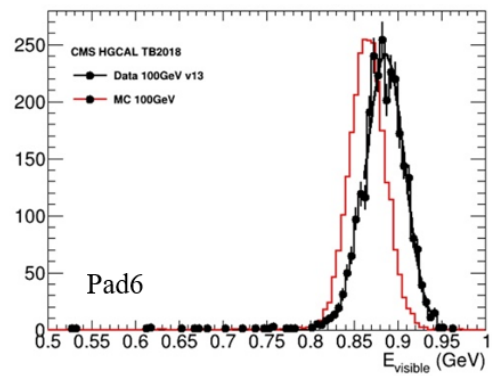
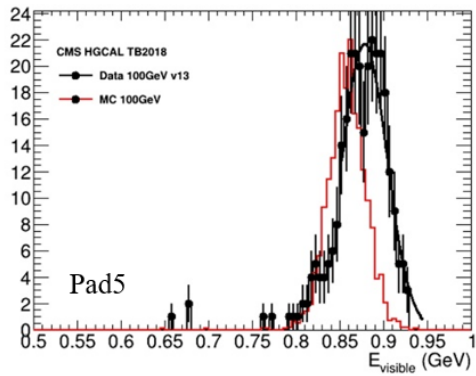
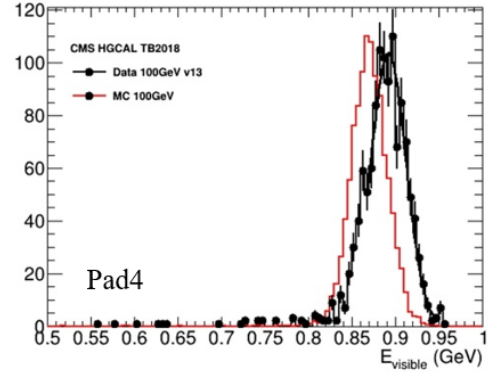
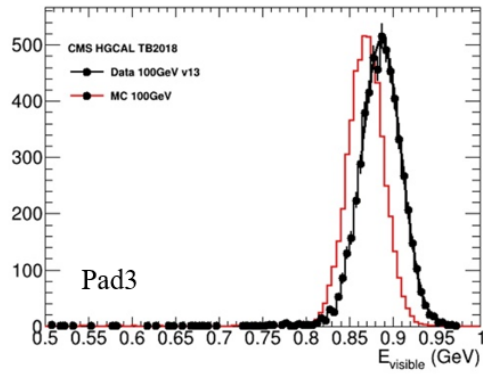
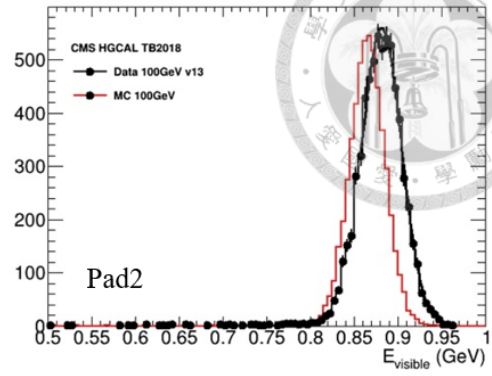
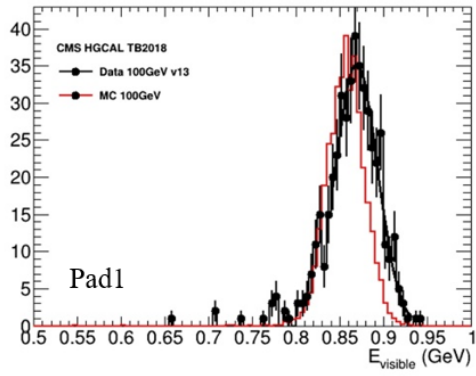




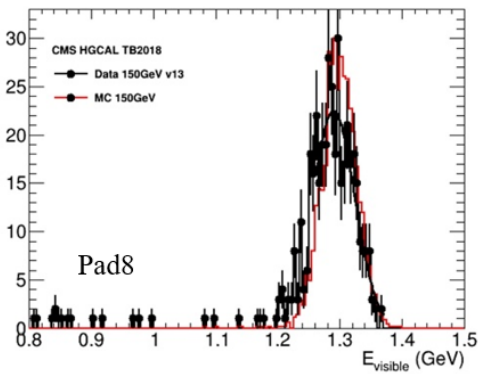
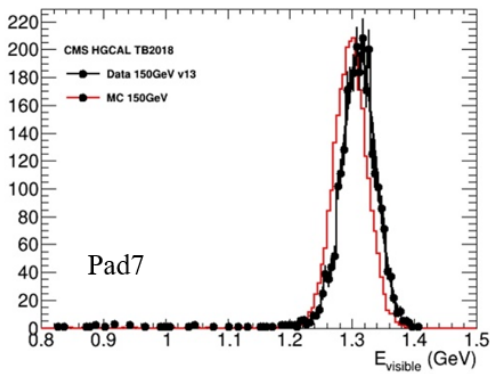
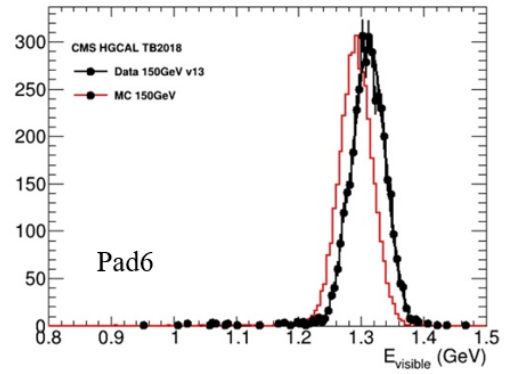
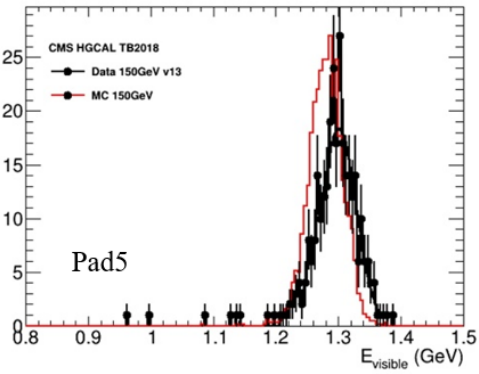
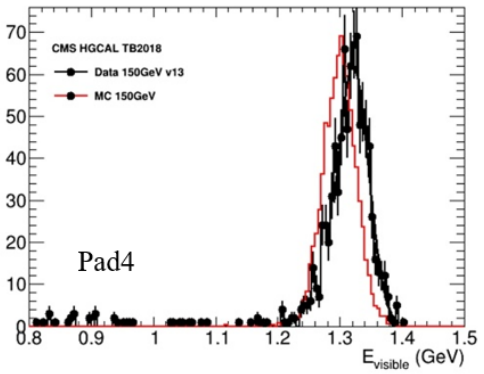
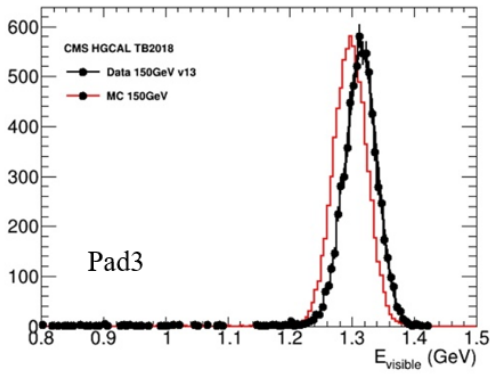
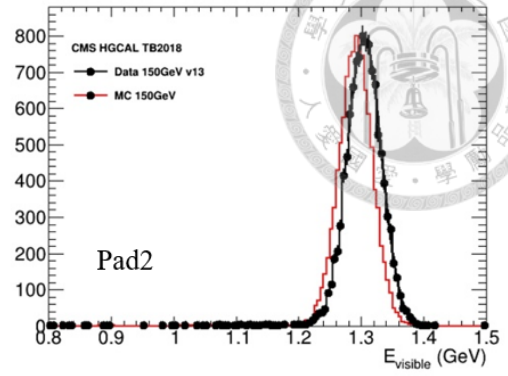
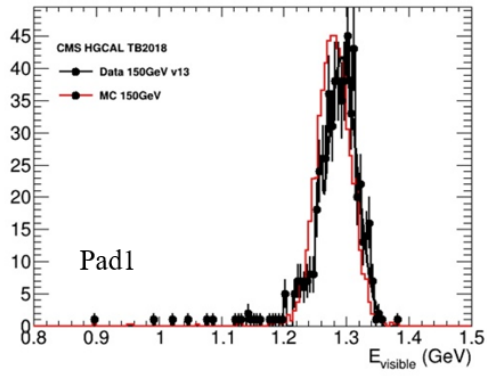
(c) 50GeV



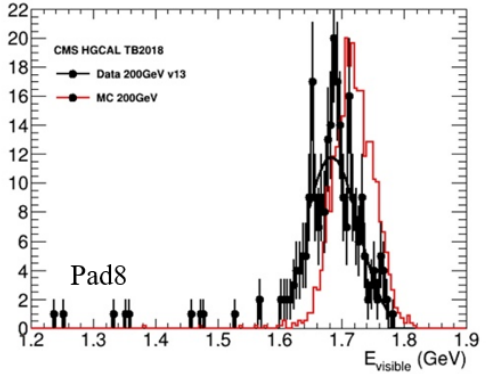
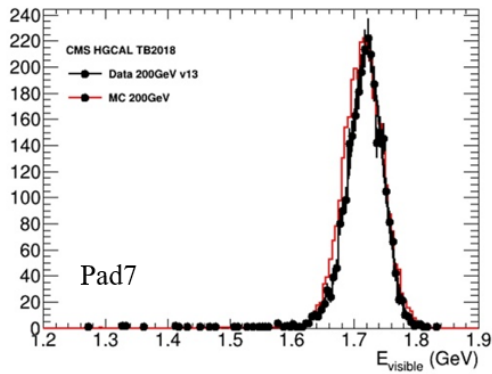
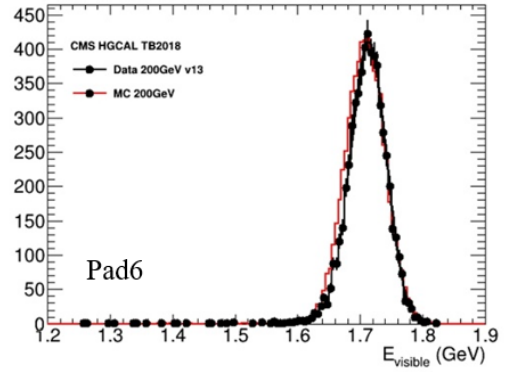
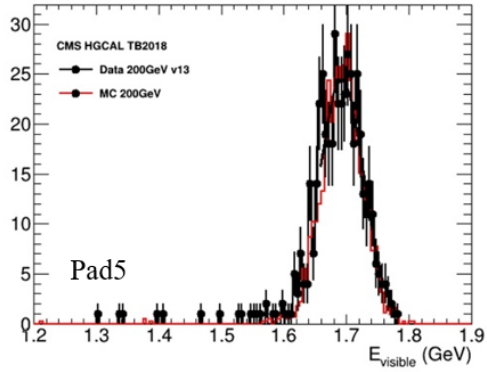
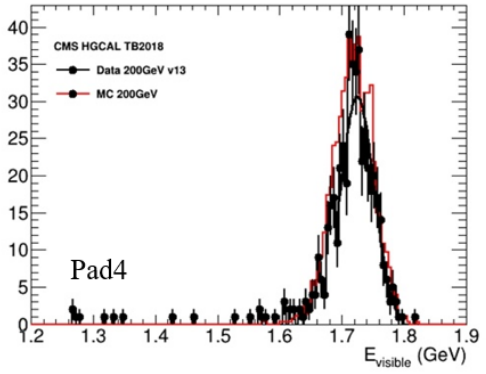
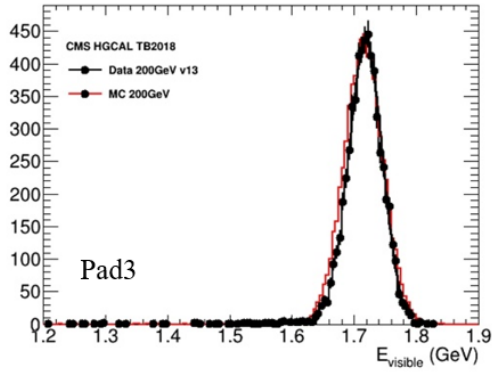
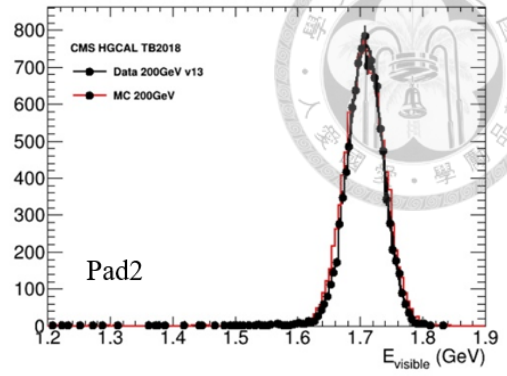
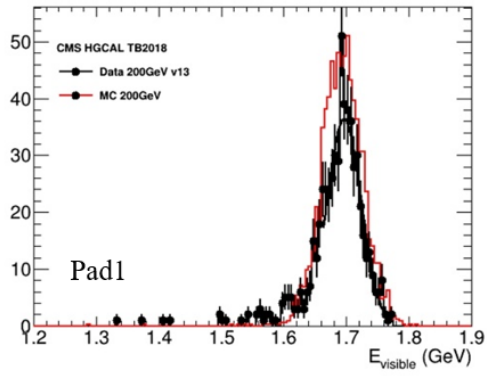
(d) 80GeV



(e) 100GeV

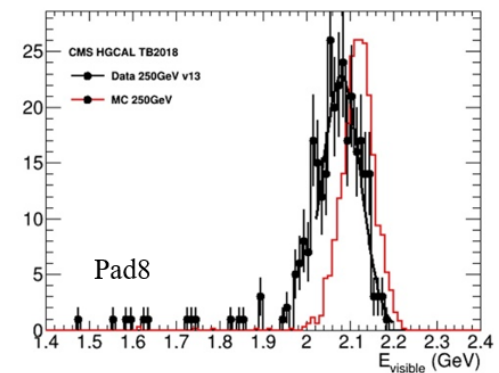
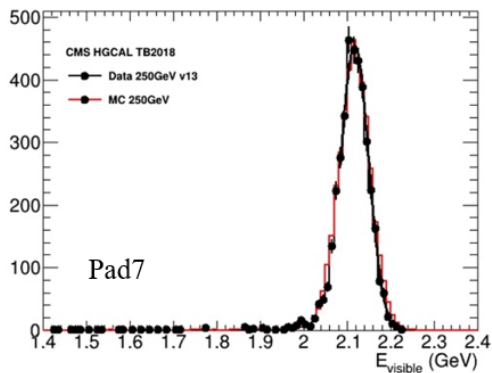
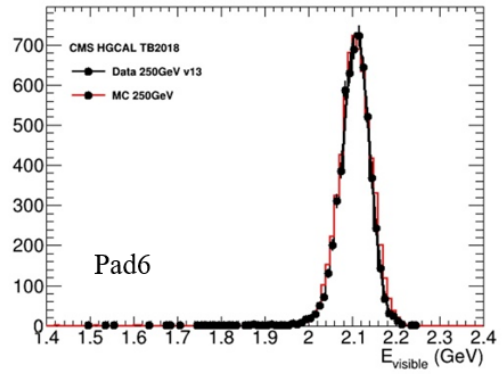
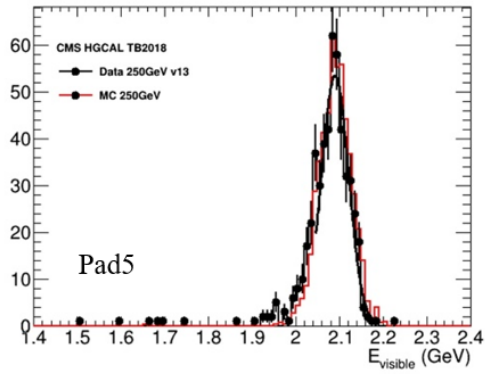
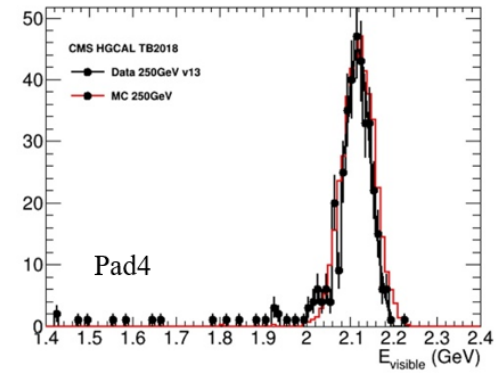
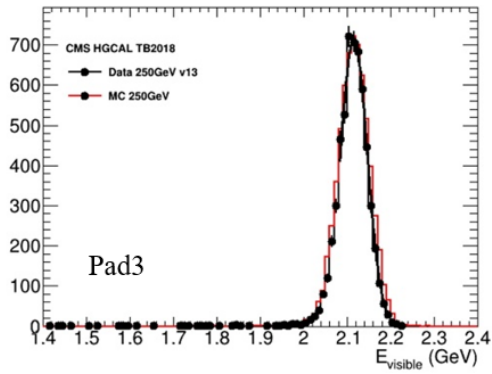
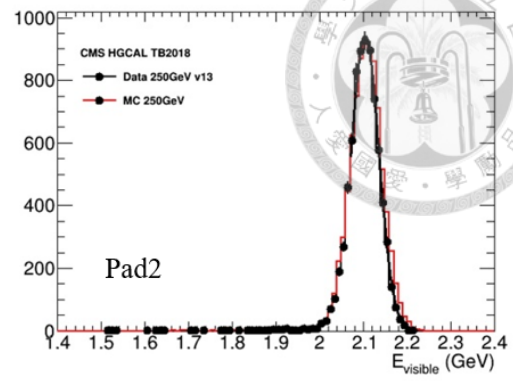
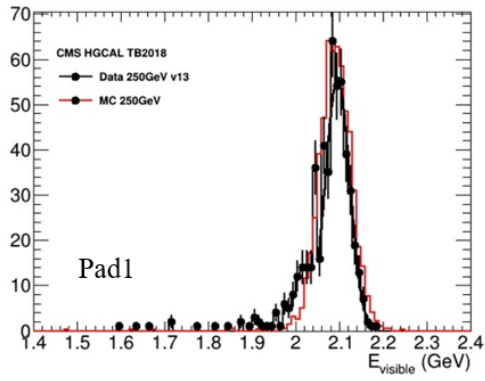


(f) 150GeV

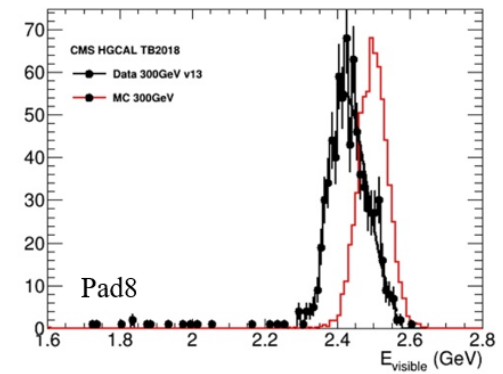
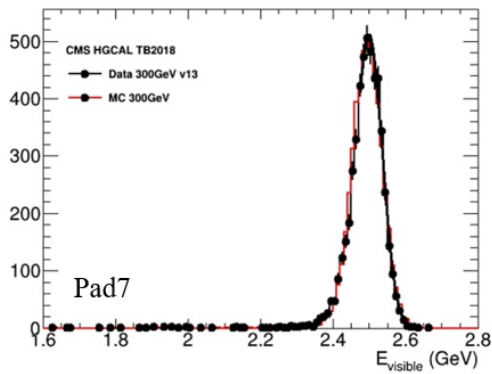
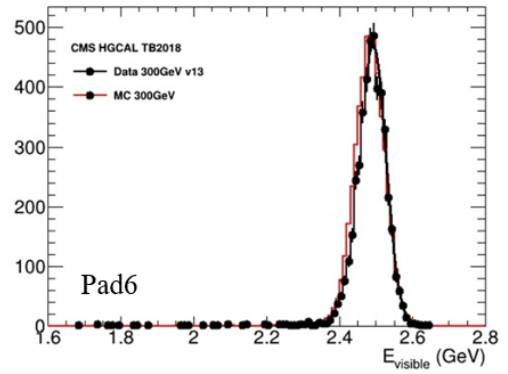
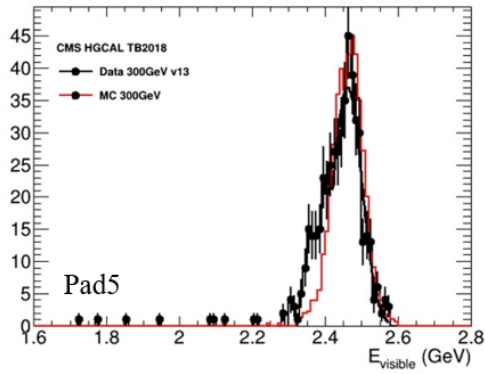
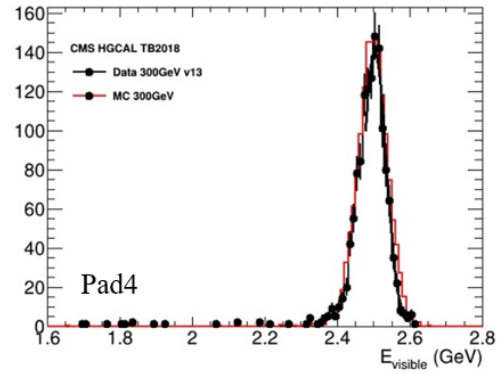
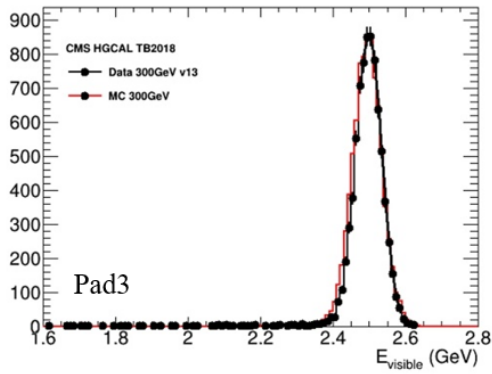
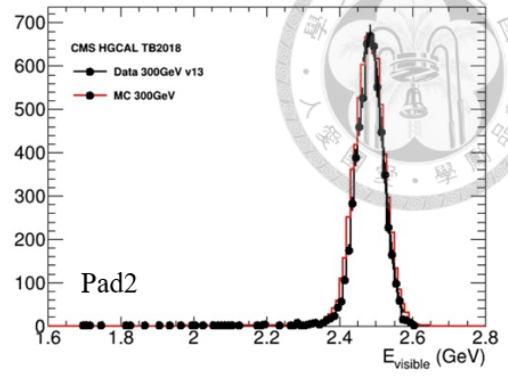
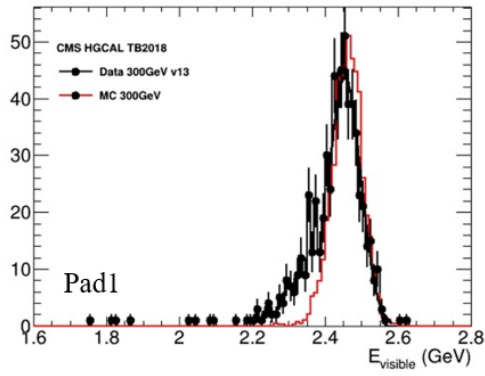


(g) 200GeV





(h) 250GeV



(i) 300GeV

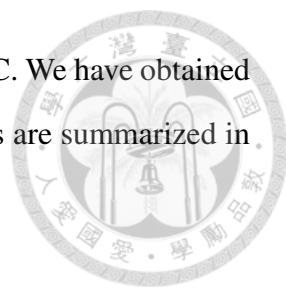
|         | All pads | 1      | 2      | 3      | 4      | 5      | 6      | 7      | 8      |
|---------|----------|--------|--------|--------|--------|--------|--------|--------|--------|
| 20 GeV  | 0.1733   | 0.1714 | 0.1740 | 0.1746 | 0.1730 | 0.1732 | 0.1730 | 0.1737 | 0.1747 |
| 30 GeV  | 0.2606   | 0.2591 | 0.2621 | 0.2628 | 0.2631 | 0.2602 | 0.2587 | 0.2593 | 0.2628 |
| 50 GeV  | 0.4349   | 0.4339 | 0.4388 | 0.4393 | 0.4402 | 0.4334 | 0.4311 | 0.4322 | 0.4400 |
| 80 GeV  | 0.6996   | 0.7043 | 0.7068 | 0.7086 | 0.7110 | 0.7038 | 0.6950 | 0.6953 | 0.7129 |
| 100 GeV | 0.8833   | 0.8690 | 0.8814 | 0.8865 | 0.8920 | 0.8783 | 0.8857 | 0.8846 | 0.8695 |
| 150 GeV | 1.3091   | 1.2927 | 1.3045 | 1.3150 | 1.3210 | 1.3004 | 1.3125 | 1.3110 | 1.2896 |
| 200 GeV | 1.7126   | 1.6964 | 1.7085 | 1.7184 | 1.7247 | 1.6922 | 1.7130 | 1.7198 | 1.6832 |
| 250 GeV | 2.1089   | 2.0954 | 2.1039 | 2.1152 | 2.1175 | 2.0897 | 2.1091 | 2.1170 | 2.0795 |
| 300 GeV | 2.4929   | 2.4534 | 2.4819 | 2.4990 | 2.5031 | 2.4609 | 2.4917 | 2.4993 | 2.4168 |

Table 4: The MPV of data  $E_{visible}(E^{Si})$  in different pads with different energies.

|        | All pad | 1      | 2      | 3      | 4      | 5      | 6      | 7      | 8      |
|--------|---------|--------|--------|--------|--------|--------|--------|--------|--------|
| 20GeV  | 0.1718  | 0.1701 | 0.1726 | 0.1734 | 0.1735 | 0.1698 | 0.1723 | 0.1731 | 0.1730 |
| 30GeV  | 0.2592  | 0.2560 | 0.2596 | 0.2602 | 0.2608 | 0.2569 | 0.2584 | 0.2602 | 0.2608 |
| 50GeV  | 0.4333  | 0.4291 | 0.4325 | 0.4352 | 0.4357 | 0.4289 | 0.4329 | 0.4354 | 0.4356 |
| 80GeV  | 0.6935  | 0.6859 | 0.6925 | 0.6956 | 0.6968 | 0.6871 | 0.6928 | 0.6959 | 0.6966 |
| 100GeV | 0.8667  | 0.8575 | 0.8658 | 0.8691 | 0.8696 | 0.8590 | 0.8654 | 0.8691 | 0.8705 |
| 150GeV | 1.2941  | 1.2804 | 1.2921 | 1.2975 | 1.3005 | 1.2808 | 1.2922 | 1.2977 | 1.2996 |
| 200GeV | 1.7104  | 1.6924 | 1.7079 | 1.7157 | 1.7199 | 1.6939 | 1.7085 | 1.7153 | 1.7184 |
| 250GeV | 2.1106  | 2.0907 | 2.1077 | 2.1162 | 2.1213 | 2.0944 | 2.1092 | 2.1184 | 2.1218 |
| 300GeV | 2.4887  | 2.4664 | 2.4844 | 2.4942 | 2.4979 | 2.4690 | 2.4848 | 2.4971 | 2.5024 |

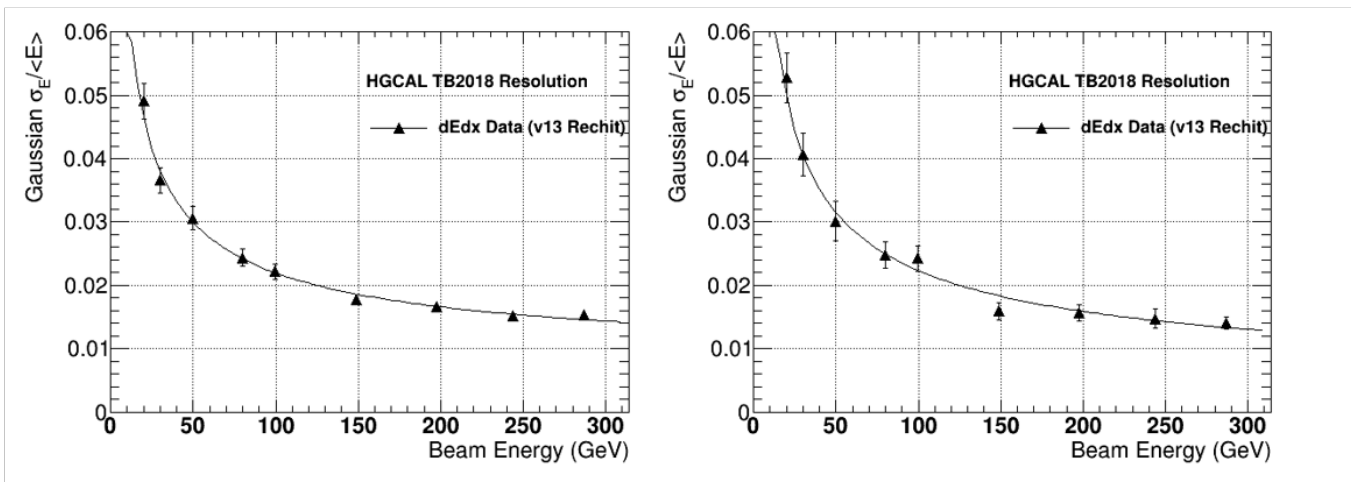
Table 5: The MPV of MC  $E_{visible}(E^{Si})$  in different pads with different energies.





In Figure energy resolution curves are shown for both data and MC. We have obtained the resolution for different pads, as well as for all pads. These results are summarized in Table 6, and also shown graphically in Figure 6.6.

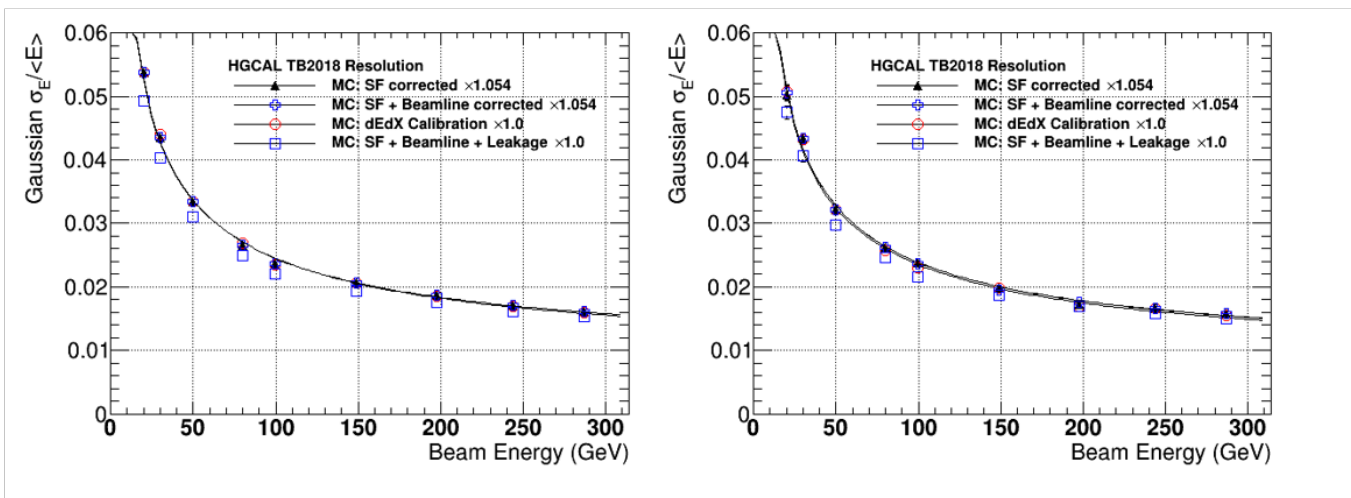
### Data



All pads

Pad4

### MC



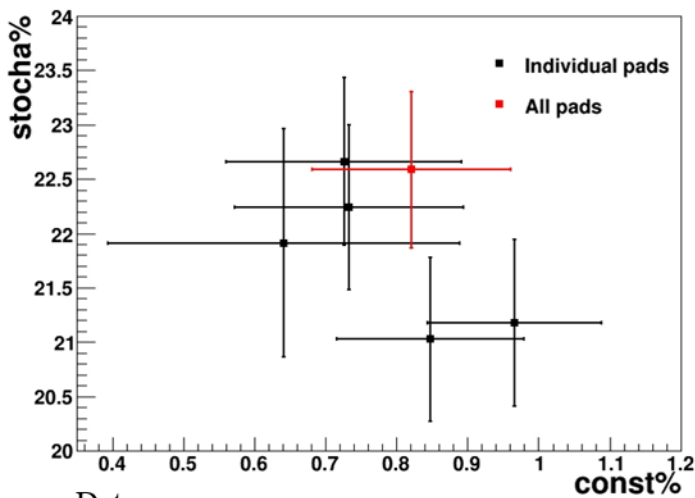
All pads

Pad4

Figure 6.5: The resolution plot of all pads and single pad for data and MC.

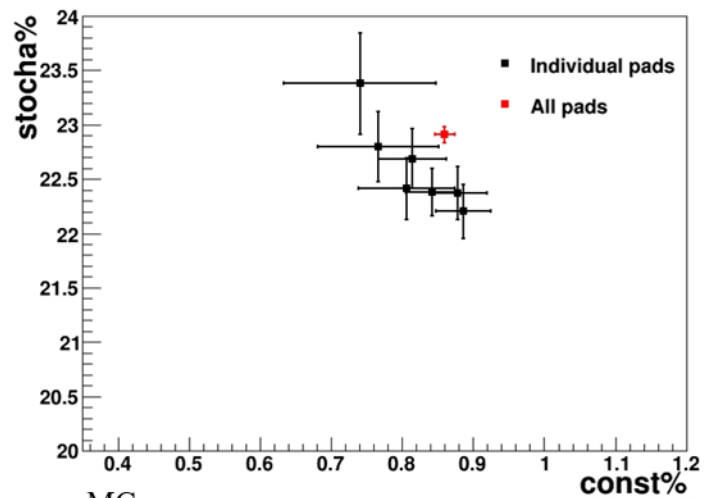
| Data |                  |                | MC  |                  |                |
|------|------------------|----------------|-----|------------------|----------------|
| pad  | Stochastic term% | Constant term% | pad | Stochastic term% | Constant term% |
| 1    | 19.59+/-1.27     | 1.01+/-0.19    | 1   | 23.38+/-0.47     | 0.74+/-0.11    |
| 2    | 21.18+/-0.77     | 0.97+/-0.12    | 2   | 22.20+/-0.25     | 0.89+/-0.04    |
| 3    | 21.03+/-0.75     | 0.85+/-0.13    | 3   | 22.38+/-0.21     | 0.84+/-0.04    |
| 4    | 21.91+/-1.05     | 0.64+/-0.25    | 4   | 22.41+/-0.28     | 0.81+/-0.07    |
| 5    | 19.02+/-1.27     | 1.30+/-0.18    | 5   | 23.26+/-0.54     | 0.50+/-0.17    |
| 6    | 22.66+/-0.77     | 0.73+/-0.17    | 6   | 22.69+/-0.27     | 0.81+/-0.05    |
| 7    | 22.24+/-0.76     | 0.73+/-0.16    | 7   | 22.37+/-0.24     | 0.88+/-0.04    |
| 8    | 17.97+/-1.36     | 2.08+/-0.16    | 8   | 22.80+/-0.32     | 0.77+/-0.08    |
| all  | 22.59+/-0.72     | 0.82+/-0.14    | all | 22.91+/-0.07     | 0.86+/-0.01    |

Table 6: The stochastic terms and constant terms of different pads in data and MC.



Data:

Mean of Const. term = 0.81 +/- 0.18 %  
 Mean of Stoch. term = 21.38 +/- 0.71 %



MC:

Mean of Const. term = 0.82 +/- 0.03 %  
 Mean of Stoch. term = 22.60 +/- 0.14 %

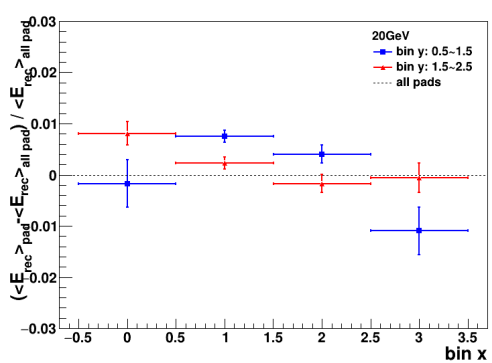
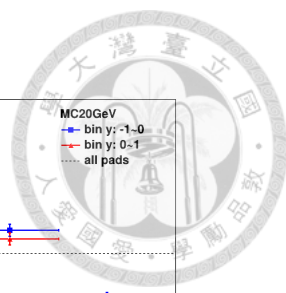
Figure 6.6: Constant term vs stochastic term for different pads.

Some of the points are removed from the graph, because for some pads there is not enough statistics. From the plots we can see that there exists an anti-correlation between

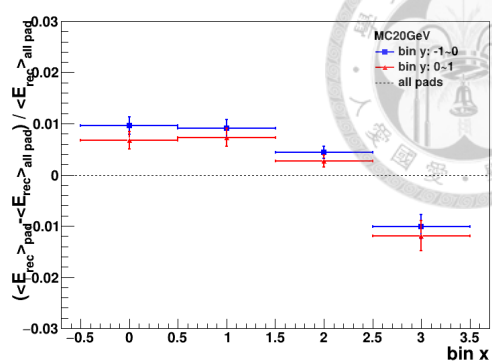
the stochastic term and the constant term. This is due to limitation in the fit, since higher energies than 300 GeV are needed in order to constrain the C-term. At the moment the minimum of the fit has a shallow direction outlined by larger values of the stochastic term and lower values of the C-term or vice versa.

These results show a reasonable agreement between data and MC, with C-term being around 0.8% for both. The question is if individual pads gives smaller C-term (what is called, local C-term), something not easy to extract from these results, due to lack of statistics.

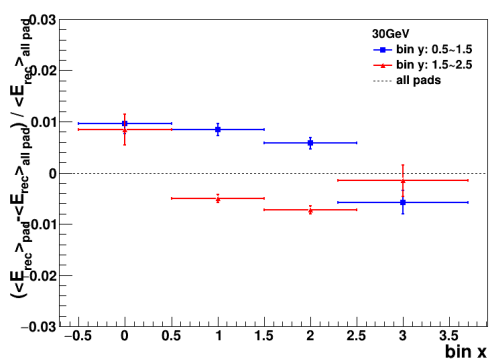
To better study the presence of pad-to-pad non-uniformity we use the  $\langle E_{visible} \rangle$  distribution for each pad, and attempt to observe any deviations for constant beam energy. The following graphs show the deviation of  $E_{visible}$  from the  $\langle E_{visible} \rangle$  for all pad. The y-axis refers to  $(\langle E_{rec} \rangle_{pad} - \langle E_{rec} \rangle_{all\ pad}) / \langle E_{rec} \rangle_{all\ pad}$  and x-axis refers to bin (pad) position. The blue matters refer to the pads 1, 2, 3 and 4, the red refer to pads 5, 6, 7 and 8. Notice that the y-error bars show the error propagated of  $E_{visible}$  from Figure 6, while the x-error bars show the width of bin (pad).



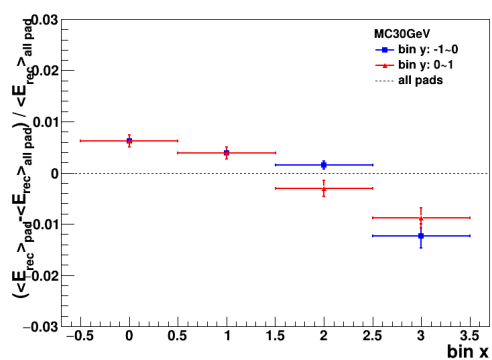
(a) data:20GeV



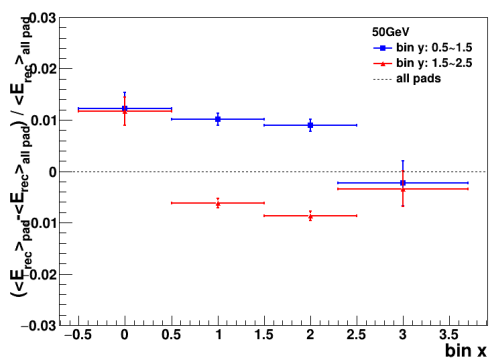
(b) MC:20GeV



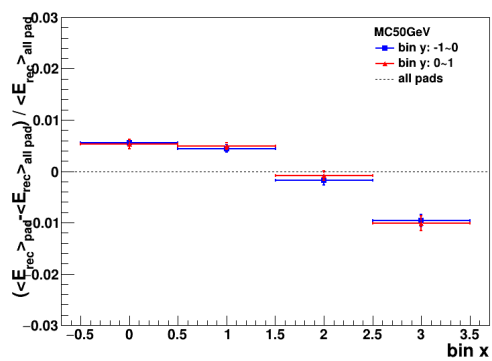
(c) data:30GeV



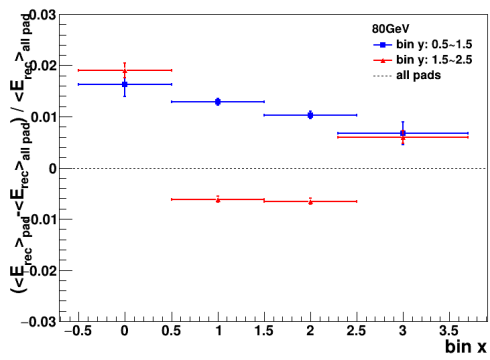
(d) MC:30GeV



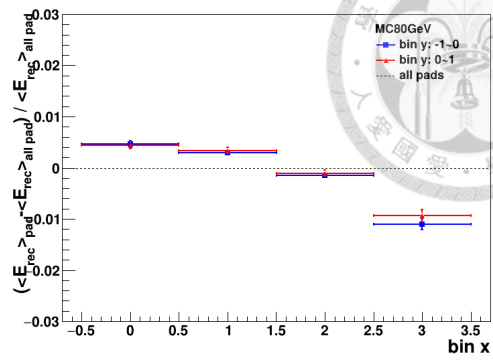
(e) data:50GeV



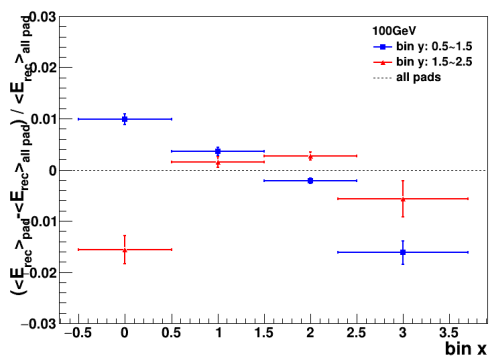
(f) MC:50GeV



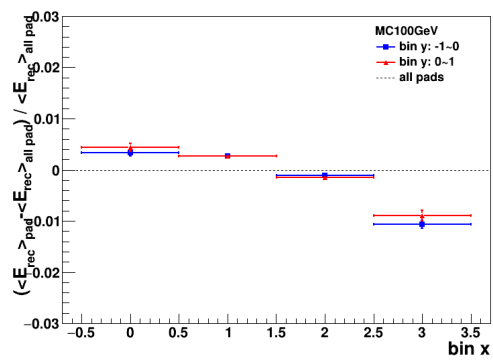
(g) data:80GeV



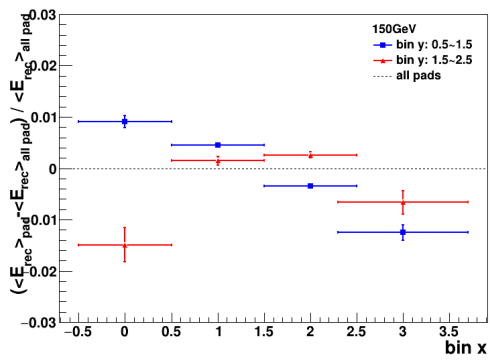
(h) MC:80GeV



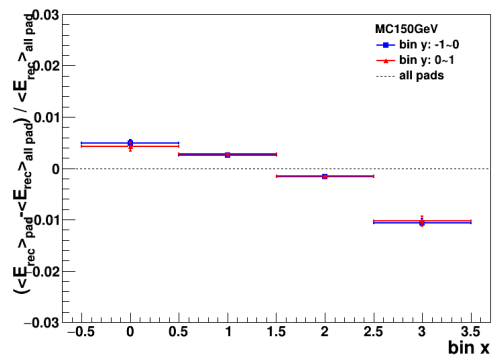
(i) data:100GeV



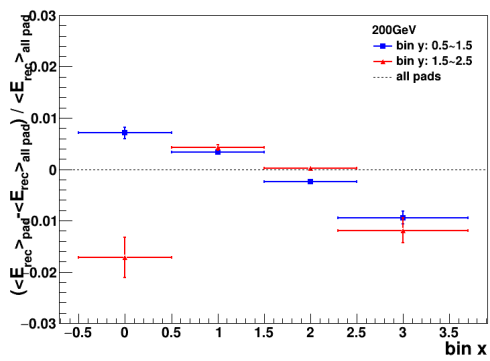
(j) MC:100GeV



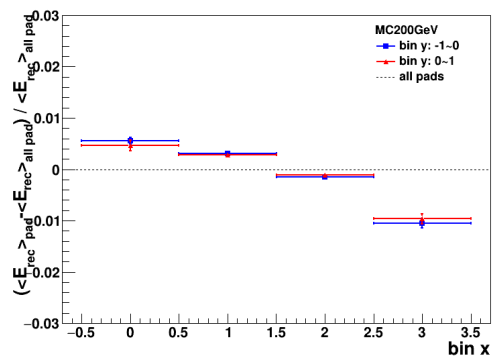
(k) data:150GeV



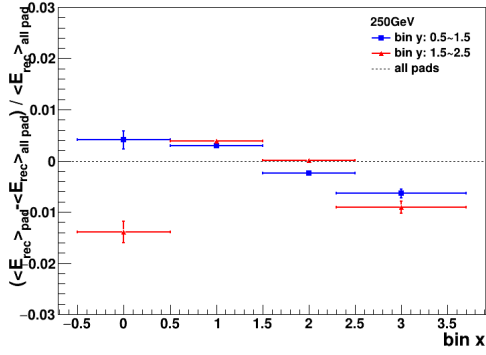
(l) MC:150GeV



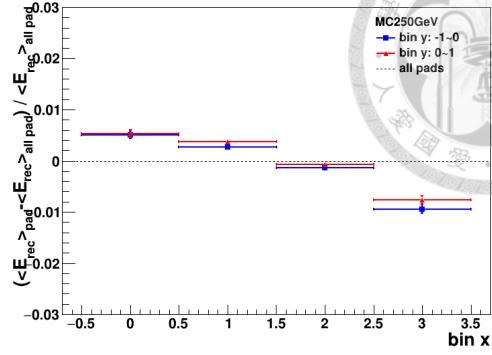
(m) data:200GeV



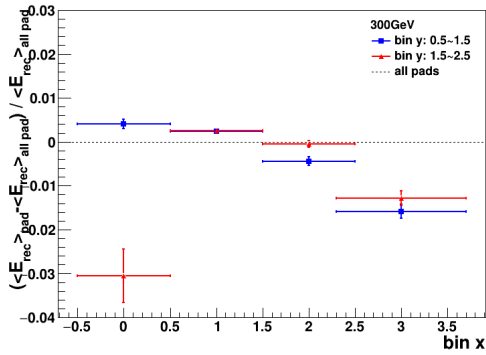
(n) MC:200GeV



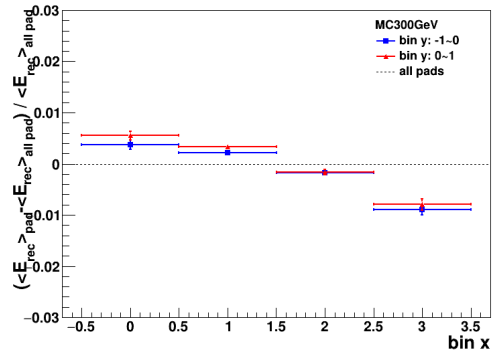
(o) data:250GeV



(p) MC:250GeV



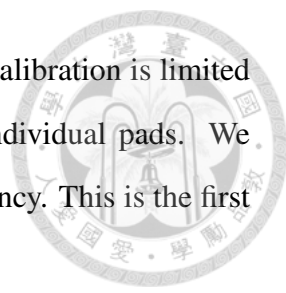
(q) data:300GeV



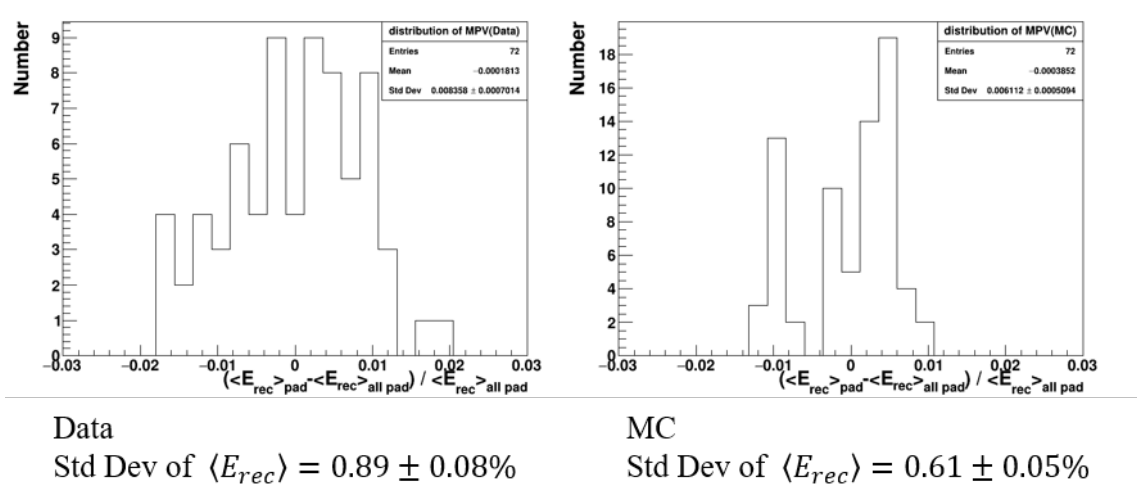
(r) MC:300GeV

Figure 6.7:  $E_{rec}$  deviation for different pads.

From these graphs we see a similar pattern of drop of response as we go away from the center of the detector. The deviations in data are in the range of 2%, and in MC are in the range of 1%. Since the detector in MC is homogeneous, this non-uniformity is not coming from difference response in the versus position. It is because as the beam moves away from the center, the shower is no longer contained in the detector, but the energy leaks from the side. Generally speaking, the trends of data and MC are the same. Measurements of this non-uniformity using the spread of the single pad  $\langle E_{rec} \rangle$  with all pads  $\langle E_{rec} \rangle$  for all 9 energies are shown in Figure 6.8. The histogram standard deviation is  $0.84 \pm 0.07$  % for data and  $0.61 \pm 0.05$  % for MC. Both data and MC show a non-uniformity, but the data shows a larger non-uniformity than MC by  $0.65 \pm 0.06$ %. This difference between data and MC is attributed to effects that MC does not include. Examples are ADC/MIP



calibration, noise effects, cross talk and electronics. The ADC/MIP calibration is limited due to statistics. It is really out of the question to the calibrate individual pads. We strongly believe that this is the main reason for the data/MC discrepancy. This is the first time that such an effect is directly evaluated.



Data  
Std Dev of  $\langle E_{rec} \rangle = 0.89 \pm 0.08\%$

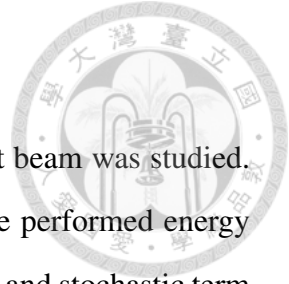
MC  
Std Dev of  $\langle E_{rec} \rangle = 0.61 \pm 0.05\%$

Figure 6.8: The distribution of the deviations from different pads in all energy.

The x-axis refers to  $\langle E_{rec} \rangle_{\text{pad}} - \langle E_{rec} \rangle_{\text{all pad}} / \langle E_{rec} \rangle_{\text{all pad}}$ . 8 pads for each energy for 9 energies, thus there are 72 points for both data and MC.

## 7 Conclusion

In this thesis the HGICAL electron energy reconstruction in 2018 test beam was studied. The 2018 test beam includes energies from 20 GeV to 300 GeV. We performed energy resolution, linearity and uniformity studies. We found a constant term and stochastic term of  $0.82 \pm 0.14\%$ ,  $22.59 \pm 0.72\%$  for data and  $0.86 \pm 0.01\%$ ,  $22.91 \pm 0.07\%$  for MC respectively. The MC is in good agreement with data. The main study in this thesis is to evaluate the electron energy uniformity of response from one pad to another pad in the prototype module for both data and MC. We found a non-uniformity  $0.89 \pm 0.08\%$  for data and  $0.61 \pm 0.05\%$  for MC, which corresponds to a  $0.65 \pm 0.06\%$  mismatch between data and MC. This discrepancy is attributed to Electronics ADC/MIP calibration limitations. Due to lack of statistics only groups of pads can be MIP/Calibrated on average and not individual pads. This leads to a position dependent effect in response.





## References



- [1] Particle Data Group collaboration, 2018.
- [2] CMS Collaboration. "The CMS experiment at the CERN LHC", 2008. doi: 10.1088/1748-0221/3/08/s08004.
- [3] R. Hadjiiska et al. P. Paolucci. "Cms resistive plate chamber overview, from the present system to the upgrade phase I". arXiv:1209.1941. doi: 10.1088/1748-0221/8/04/P04005.
- [4] <https://project-hl-lhc-industry.web.cern.ch/content/project-schedule>.
- [5] HGCAL Beam test group. "First beam tests of prototype silicon modules for the CMS High Granularity Endcap Calorimeter".
- [6] CMS collaboration. "The Phase-2 Upgrade of the CMS Endcap Calorimeter Technical design report". CERN-LHCC-2017-023.
- [7] Richard C. Fernow. "Introduction to experimental particle physics", 1986.
- [8] Rende Steerenberg. "LHC Report: The LHC is full!", 2018. <https://home.cern/tags/lhc-report>.
- [9] CMS Collaboration. "Technical Proposal for the upgrade of the CMS Detector through 2020". CMS UG-TP1.
- [10] William R. Leo. "Techniques for Nuclear and Particle Physics Experiment", 1987.
- [11] "H2 beam line". <http://sba.web.cern.ch/sba/BeamsAndAreas/h2/H2manual.html>.
- [12] J. Borg et al. "SKIROC2.CMS an ASIC for testing CMS HGCAL", feb 2017. doi: 10.1088/1748-0221/12/02/c02019.

- [13] D. Barney. "Construction, Commissioning and Calibration of Cms HGICAL prototype 887 silicon modules". to be published in JINST (2019).
- [14] P. Ahlburg et al. "EUDAQ - Data Acquisition Software Framework for Common Beam Telescopes". arXiv:1909.13725.

